

# Insights into the long-term (2005-2021) spatiotemporal evolution of summer ozone production sensitivity in the Northern Hemisphere derived with OMI

Matthew S. Johnson<sup>1\*</sup>, Sajeev Philip<sup>2</sup>, Scott Meech<sup>3</sup>, Rajesh Kumar<sup>3</sup>, Meytar Sorek-Hamer<sup>4</sup>, Yoichi P. Shiga<sup>4</sup>, Jia Jung<sup>1,5</sup>

<sup>1</sup>Earth Science Division, NASA Ames Research Center, Moffett Field, CA 94035, USA

<sup>2</sup>Centre for Atmospheric Sciences, Indian Institute of Technology Delhi, New Delhi, India

<sup>3</sup>Research Applications Laboratory, NSF National Center for Atmospheric Research, Boulder, CO 80305, USA

<sup>4</sup>NASA Academic Mission Services by Universities Space Research Association at NASA Ames Research Center, Mountain View, CA, USA

<sup>5</sup>Bay Area Environmental Research Institute, Moffett Field, CA 94035, USA

\*Correspondence: Matthew S. Johnson (matthew.s.johnson@nasa.gov)

**Abstract.** Tropospheric ozone ( $O_3$ ) formation depends on the relative abundance of precursor species, nitrogen oxides ( $NO_x$ ) and volatile organic compounds (VOCs). Advancements in satellite retrievals of formaldehyde (HCHO) and nitrogen dioxide ( $NO_2$ ) vertical column densities (VCDs), and the corresponding HCHO/ $NO_2$  ratios (FNRs), provide the opportunity to diagnose the spatiotemporal evolution of  $O_3$  production sensitivity regimes. This study investigates trends of summertime VCD HCHO,  $NO_2$ , and Ozone Monitoring Instrument (OMI)-derived FNRs in the Northern Hemisphere from 2005 to 2021. FNR trends were analysed for polluted regions, specifically for 46 highly populated cities, over the entire 17-year period and in 2020 when global anthropogenic emissions were reduced due to COVID-19 lockdown restrictions. It was determined that OMI-derived FNRs have increased on average ~65% across cities in the Northern Hemisphere. Increasing OMI-derived FNRs indicates a general transition from radical-limited to  $NO_x$ -limited regimes. The increasing trend is driven by reduced  $NO_2$  concentrations because of emission control strategies of  $NO_x$ . OMI FNR trends were compared to ground-based in situ measurements in US cities and determined they can capture the trends in increasing FNRs ( $R = 0.91$ ) and decreasing  $NO_2$  ( $R = 0.98$ ) occurring at the surface. OMI FNRs in urban areas were higher (~20%) in 2020 for most cities studied here compared to 2019 and 2021. In addition to studying the longest period of OMI FNRs across the Northern Hemisphere to-date, the capabilities and challenges of using satellite VCD FNRs to study surface-level  $O_3$  production sensitivity regimes are discussed.

**Short Summary.** Satellites, such as the Ozone Monitoring Instrument (OMI), retrieve proxy species of ozone ( $O_3$ ) formation (formaldehyde and nitrogen dioxide) and the ratios (FNRs) which can define  $O_3$  production sensitivity regimes. Here we investigate trends of OMI FNRs from 2005 to 2021 and they have increased in major cities suggesting a transition from radical- to nitrogen oxide-limited regimes. OMI also observed the impact of reduced emissions during the 2020 COVID-lockdown resulting in increased FNRs.

## 1 Introduction

Tropospheric ozone ( $O_3$ ) is a harmful pollutant which has detrimental impacts on air quality leading to adverse human health and premature mortality, and negative impacts on vegetation and agriculture (US EPA, 2006; Tai et al., 2014; GMD, 2020). A myriad of volatile organic compounds (VOCs) can be photochemically oxidized through a complex series of chemical reactions involving nitrogen oxides ( $NO_x =$  nitric oxide [NO] + nitrogen dioxide [ $NO_2$ ]) which leads to tropospheric  $O_3$  formation (Haagen-Smit, 1952; Monks et al., 2015; Seinfeld and Pandis, 2016). The complex  $O_3$ - $NO_x$ -VOC chemical relationship results in local nonlinear  $O_3$

38 formation which is sensitivity to the relative abundances of its precursor species ( $\text{NO}_x$  and VOCs), generally categorized as “ $\text{NO}_x$ -  
39 limited” versus “radical-limited” photochemical regimes (Sillman et al., 1990; Kleinman, 1994). In a  $\text{NO}_x$ -limited regime, local  
40  $\text{O}_3$  production increases/decreases with increased/reduced  $\text{NO}_x$  emissions and concentrations, with no impact from VOC  
41 perturbations. Whereas in a radical-limited regime (also known as “VOC-limited”, “hydrocarbon-limited”, or “ $\text{NO}_x$ -saturated”)  
42 the formation of local  $\text{O}_3$  increases/decreases with increased/reduced VOC emissions and concentrations; however, can also  
43 slightly be impacted by  $\text{NO}_x$  emission and concentration changes. The accurate knowledge of regional and local  $\text{O}_3$  photochemical  
44 regimes is critical for developing emission control strategies to reduce surface  $\text{O}_3$  concentrations. Overall, studying the  
45 spatiotemporal evolution of the nonlinear  $\text{O}_3$ - $\text{NO}_x$ -VOC chemistry is critical to policy decision making (National Research Council,  
46 1991) and important as a fundamental scientific problem (Sillman, 1999).

47 Diagnosing regional and local  $\text{O}_3$  photochemical regimes has always been recognized as a challenging task. Measurements  
48 of proxy or indicator species (e.g., total reactive nitrogen, HCHO, hydrogen peroxide, nitric acid), and estimating the correlations  
49 of such species, are the observation-based or model-observation synthesis approaches to detect  $\text{O}_3$  sensitivity regimes (Sillman,  
50 1995; Jacob et al., 1995; Tonnesen and Dennis, 2000). These measurements and associated studies are typically limited to field  
51 campaign time periods and locations which hinders the spatiotemporal coverage of such data posing an obstacle for investigating  
52 global and regional  $\text{O}_3$  production sensitivity over multi-year time periods. The response of  $\text{O}_3$  formation to changes in precursor  
53 emissions can also be assessed through modeling approaches such as source apportionment studies (Li et al., 2012), forward model  
54 sensitivity simulations (Wu et al., 2009), and simulations using adjoint model capabilities (Zhang et al., 2009). However,  
55 uncertainties inherent in model predictions of  $\text{O}_3$  physicochemical processes are a critical issue. Milford et al. (1994) and Sillman  
56 (1995) first introduced the concept of detecting photochemical regimes using the ratio of ambient concentrations of two “indicator  
57 species” HCHO to  $\text{NO}_2$  (hereafter indicator species refers to HCHO and  $\text{NO}_2$ ; the ratio of these two species as FNR), which can  
58 be used to represent VOCs and  $\text{NO}_x$  which are directly involved in  $\text{O}_3$ - $\text{NO}_x$ -VOC chemistry and are readily measured via in situ  
59 sampling and satellite remote-sensing techniques. These two indicator species are the most suitable candidates for tropospheric  
60 column and planetary boundary layer (PBL)  $\text{O}_3$  sensitivity analysis using satellites due to: 1) the sensitivity of nadir-looking  
61 satellites to boundary layer FNRs, 2) most other indicator species (e.g., hydrogen peroxide, VOCs other than HCHO) cannot be  
62 readily measured via satellites and the retrievals of those species having less sensitivity to surface conditions (e.g., limb-scanning  
63 satellites), and 3) the short atmospheric lifetime of HCHO and  $\text{NO}_2$  allowing these species to be suitable for proxies of surface  
64 emissions of  $\text{NO}_x$  and VOCs.

65 Surface and PBL  $\text{O}_3$  production sensitivity diagnosed with the in situ measurements of FNRs (although sparse in spatial  
66 and temporal coverage) should be more accurate compared to satellite-based approaches of retrieving column-integrated  
67 concentrations (Schroeder et al., 2017); however, the spatiotemporal coverage of polar orbiting satellites is a clear advantage over  
68 in situ techniques. The advancements in satellite remote-sensing over the last two decades, to retrieve HCHO and  $\text{NO}_2$  vertical  
69 column density (VCD) data (Burrows et al., 1999; González Abad et al., 2019), have emerged as a new observation-based tool to  
70 detect the spatiotemporal evolution of  $\text{O}_3$  sensitivity from a global- to local-scale (Martin et al., 2004; Jin et al., 2020). Martin et  
71 al. (2004) first demonstrated the capability of FNR VCDs from the Global Ozone Monitoring Experiment (GOME) satellite to  
72 detect photochemical regimes. Subsequently, this technique was adopted by more studies using other satellite instruments such as  
73 Ozone Monitoring Instrument (OMI), GOME-2, and TROPospheric Monitoring Instrument (TROPOMI) (Duncan et al., 2010;  
74 Witte et al., 2011; Choi et al., 2012; Choi and Souri, 2015; Chang et al., 2016; Jin and Holloway 2015; Souri et al., 2017; Jin et  
75 al., 2017; 2020; Wang et al., 2021; Tao et al., 2022; Johnson et al., 2023; Acdan et al., 2023) up to a point that the results have  
76 been suggested to potentially be used to inform State-Implementation Plans (SIP) in the United States (US) (Jin et al., 2018).  
77 However, the accurate diagnosis of surface  $\text{O}_3$  sensitivity regimes is impeded by numerous uncertainty components which can be

78 broadly classified into two major categories: 1) inherent uncertainties associated with the approach of relating indicator species to  
79 diagnose local O<sub>3</sub> sensitivity at a location/time period, and 2) uncertainties associated with satellite-retrieved column-integrated  
80 concentrations of indicator species to infer surface O<sub>3</sub> sensitivity. The former uncertainty arises from numerous factors: difficulties  
81 in identifying accurate FNR “threshold” values (hereafter, “threshold” refers to threshold ratio values) separating different O<sub>3</sub>  
82 sensitivity regimes over a location and time period (Schroeder et al., 2017; Jin et al., 2017), dependency of ambient O<sub>3</sub> and its  
83 formation to factors other than precursor species such as water vapor, meteorology, deposition, transport, and aerosol interaction  
84 (e.g., Kleinman et al., 2005; Camalier and Dolwick, 2007), varying sensitivity of HCHO VCD data to anthropogenic VOCs (Jin et  
85 al., 2020), and dependence of NO<sub>2</sub> in the production of ambient HCHO concentrations (Souri et al., 2020). These inherent  
86 uncertainty sources limit the utility of satellite-based data for diagnosing O<sub>3</sub> sensitivity regimes. Fortunately, recent studies have  
87 investigated these discrepancies in the methodology of using satellite-derived FNRs to infer O<sub>3</sub> sensitivity regimes using data from  
88 airborne campaign data and 0-D photochemical box models (e.g., Schroeder et al., 2017; Souri et al., 2020; Souri et al., 2023a).

89 This study investigates 17 years (2005-2021) of OMI satellite sensor data which provides consistent near daily global  
90 coverage of VCD retrievals of HCHO and NO<sub>2</sub> (Levelt et al., 2018) that are well suited to investigate the long-term spatiotemporal  
91 evolution of O<sub>3</sub> sensitivity regimes. Numerous studies have used OMI VCD data up to the year 2016 to assess the trends in FNR  
92 values over specific regions, mostly over the US and East Asia (Mahajan et al., 2015; Jin and Holloway, 2015; Souri et al., 2017;  
93 Jin et al., 2017, 2020). Extending the OMI data set out to 2021 is novel and allows for the investigation of COVID-19 lockdown  
94 restrictions on FNRs throughout the Northern Hemisphere. In this study we investigate the capability of VCD HCHO, NO<sub>2</sub>, and  
95 FNR data from OMI to reflect the trends in PBL and surface level O<sub>3</sub> production sensitivity regimes. We do not calculate actual  
96 magnitudes of surface HCHO, NO<sub>2</sub>, and FNRs derived with OMI VCD data as these proxy products are heavily reliant on chemical  
97 transport models (CTMs) and spatiotemporally sparse ancillary information, both sources which have large uncertainties (discussed  
98 in Sect. 4). Satellite retrieval errors can be reduced by averaging satellite data temporally (seasonal, annual, or multi-year means)  
99 and spatially (by averaging individual satellite pixels across 10’s to 100’s of kilometers), although such averaging approaches  
100 preclude the analysis of O<sub>3</sub> sensitivity regimes at high spatiotemporal scales. Several studies have therefore focused on assessing  
101 O<sub>3</sub> production sensitivity using spatially-averaged satellite data aggregated to monthly, seasonal, or multi-year means over large  
102 areas (e.g., Jin et al., 2020). In this study, we investigate the long-term changes in summer-mean (June, July, and August [JJA])  
103 VCD FNRs across numerous polluted cities (cities with high NO<sub>2</sub> VCDs) in the Northern Hemisphere. This manuscript is structured  
104 in the following way. Section 2 describes the OMI retrievals, surface concentration measurements, “bottom-up” emission  
105 inventories, and the approach to conduct spatiotemporal variability and trend analysis. In Sect. 3, we describe the comparison of  
106 satellite VCD FNRs to surface measurements and the analysis of OMI-derived FNR values over Northern Hemisphere cities.  
107 Section 4 discusses the capabilities and issues with applying satellite-derived FNRs for studying O<sub>3</sub> production sensitivity and  
108 concluding remarks are provided in Sect. 5.

## 109 **2. Materials and methods**

### 110 **2.1 OMI satellite sensor**

111 The OMI sensor is a Dutch-Finnish built payload on the NASA Earth Observing System Aura satellite. The Aura platform flies as  
112 part of the Afternoon-Train satellite constellation along a sun-synchronous polar Low Earth Orbit (Schoeberl et al., 2006). Aura  
113 passes through the sunlit part of the Earth 14 times a day with a local overpass time of ~1:45 p.m. at the equator with near-complete  
114 daily global coverage (Levelt et al., 2006). OMI is a nadir-viewing solar backscatter grating spectrograph which takes retrievals in  
115 the ultraviolet (264–311 nm [UV1] and 307–383 nm [UV2]) and visible (349–504 nm) wavelengths (Levelt et al., 2006, 2018;  
116 Schenkeveld et al., 2017). The OMI instrument has a swath width of 2,600 km (60 pixels across track) with near-nadir spatial

117 resolution of 13 km (along-track)  $\times$  24 km (cross-track) and near-swath edge pixel size of 40 km  $\times$  250 km. OMI has been widely  
118 used by the atmospheric science, air quality, and health impact assessment communities since its launch on July 15, 2004 (e.g.,  
119 Levelt et al., 2018). The “row anomaly” appeared starting in May 2007 affecting the data quality of certain rows of OMI pixels  
120 (Dobber et al., 2008, Schenkeveld et al., 2017) and is avoided in the data products used in this study.

### 121 **2.1.1 OMI HCHO**

122 This study applies the NASA-released operational OMI HCHO version 3 collection 3 (OMHCHO) gridded level 3 (L3) VCD data  
123 at a spatial resolution of  $0.1^\circ \times 0.1^\circ$  latitude  $\times$  longitude using the Smithsonian Astrophysical Observatory (SAO) retrieval  
124 algorithm (González Abad et al., 2015). The OMHCHO retrieval applies a nonlinear fitting to the OMI-measured backscattered  
125 radiances in the UV2 spectral window following the Basic Optical Absorption Spectroscopy method (Chance, 1998) to get slant  
126 column densities (SCDs). The SCDs are then converted to VCDs by applying the air mass factor (AMF) formulation of Palmer et  
127 al. (2001), with scattering weights calculated using the Linearized Discrete Ordinate Radiative Transfer version 2.4RT (VLIDORT)  
128 Radiative Transfer Model (RTM) (Spurr, 2006) and HCHO shape factors simulated using the GEOS-Chem global CTM at a spatial  
129 resolution of  $2^\circ \times 2.5^\circ$  latitude  $\times$  longitude. The OMHCHO VCD product has a postprocessing bias correction (De Smedt et al.,  
130 2008) applied by comparing daily HCHO VCDs with background VCDs simulated with GEOS-Chem over a clean region in the  
131 Pacific Ocean (González Abad et al., 2015). González Abad et al. (2015) estimated the uncertainty of the OMHCHO product  
132 ranging from 45% to 105%, with relative contributions from the slant column retrievals (45% – 100%) and AMF calculations  
133 (~35%). Model evaluation studies have shown that CTMs have errors and uncertainties in their predictions of HCHO in the clean  
134 regions of the Pacific Ocean which could also contribute to overall OMI HCHO bias/errors (Anderson et al., 2017). Validation of  
135 OMHCHO with aircraft-based observations indicates a high bias (66.1% – 112.1%) for HCHO-poor environments and low bias (-  
136 44.5% – -21.7%) for HCHO-rich environments (Zhu et al., 2016, 2020; Johnson et al., 2023). The OMHCHO product has been  
137 used widely for estimating trends of VOC emissions (e.g., Marais et al., 2012; Shen et al., 2019) and inferring surface HCHO  
138 concentrations (Zhu et al., 2017a).

### 139 **2.1.2 OMI NO<sub>2</sub>**

140 The NASA-released standard OMI NO<sub>2</sub> (OMNO2) version 4 collection 3 gridded L3 high resolution VCD data at the spatial  
141 resolution of  $0.1^\circ \times 0.1^\circ$  latitude  $\times$  longitude was applied in this study (Lamsal et al., 2015; Krotkov et al., 2017). The OMNO2  
142 retrieval uses the Differential Optical Absorption Spectroscopy method (Marchenko et al., 2015) to derive tropospheric SCDs by  
143 spectrally fitting OMI-detected backscattered radiance in the visible wavelength window with a pseudo reference spectrum  
144 (Chance and Spurr, 1997). The stratospheric contribution of the SCD is then subtracted and the residual tropospheric SCDs are  
145 then converted to tropospheric VCDs by applying an AMF based on scattering weights calculated using the Total Ozone Mapping  
146 Spectrometer (TOMS) radiative transfer model (TOMRAD) (Dave, 1964) and shape factor profiles simulated using the Global  
147 Modeling Initiative (GMI) CTM at a spatial resolution of  $1^\circ \times 1.25^\circ$  latitude  $\times$  longitude (Krotkov et al., 2017). The uncertainty of  
148 the OMNO2 VCD product varies with cloudiness and pollution levels but is in the range of ~20% – 60% (Bucsela et al., 2013),  
149 with relative contributions from the spectral fitting (~10% over polluted regions, Boersma et al., 2011), stratospheric correction  
150 (<5%), and AMF calculations (10% – 20%). The OMNO2 product has been used for a wide range of applications including the  
151 estimation of spatiotemporal variability and trends of NO<sub>x</sub> emissions (e.g., Krotkov et al., 2016), NO<sub>2</sub> surface concentrations (e.g.,  
152 Kharol et al., 2015; Lamsal et al., 2015), information about atmospheric particulate organic matter (Philip et al., 2014), and surface  
153 O<sub>3</sub> sensitivity regime detections (e.g., Duncan et al., 2010; Jin et al., 2017).

### 154 2.1.3 Calculation of VCD FNR values

155 The daily L3 OMHCHO and OMNO2 products were filtered and processed for calculating FNR values. Both the operational  
156 products were already filtered for daily VCDs with an effective cloud fraction >30%, solar zenith angle >70% (for HCHO) and  
157 >85% (for NO<sub>2</sub>), removing pixels affected by row anomalies, and Level 2 data quality flags not designated as good (see more  
158 details in the user's guides for OMNO2 [[https://disc.gsfc.nasa.gov/datasets/OMNO2d\\_003/summary](https://disc.gsfc.nasa.gov/datasets/OMNO2d_003/summary)] and OMHCHO  
159 [[https://acdisc.gesdisc.eosdis.nasa.gov/data/Aura\\_OMI\\_Level3/OMHCHOd.003/doc/README\\_OMHCHOd\\_v003.pdf](https://acdisc.gesdisc.eosdis.nasa.gov/data/Aura_OMI_Level3/OMHCHOd.003/doc/README_OMHCHOd_v003.pdf)]).

160 During this study, we avoided unrealistically large positive and negative values for both indicator species which occur due to  
161 uncertainties in slant column retrievals and the calculation of tropospheric VCDs. We followed Zhu et al. (2020) to filter out HCHO  
162 daily VCDs outside the range of  $-8.0 \times 10^{15}$  molecules/cm<sup>2</sup> to  $7.6 \times 10^{16}$  molecules/cm<sup>2</sup>. The OMNO2 L3 product already included  
163 an upper limit of  $1 \times 10^{17}$  molecules/cm<sup>2</sup> and we applied a lower limit of  $-1 \times 10^{15}$  molecules/cm<sup>2</sup> below which NO<sub>2</sub> VCD are  
164 assumed in this study to be unrealistic. After data filtering, OMI VCD FNRs are calculated by taking the ratio of HCHO:NO<sub>2</sub> for  
165 each grid of the summer-mean products.

### 166 2.2 Surface measurement data

167 To determine if OMI VCD FNRs can replicate the trends of PBL and surface-level FNRs, long-term trends in OMI-derived VCD  
168 HCHO and NO<sub>2</sub> are compared to in situ measurement data from the United States Environmental Protection Agency's Air Quality  
169 System (US EPA AQS; <https://www.epa.gov/aqs>). We focus this evaluation on the US due to the much denser in situ measurement  
170 networks compared to other global regions. Hourly data from the EPA AQS NO<sub>2</sub> data were averaged daily from 1 pm to 3 pm  
171 local time to be consistent with the OMI overpass time. Since there is insufficient hourly data for HCHO from the EPA AQS  
172 network, we use 24-hour average data for the HCHO evaluation which is provided by the EPA. AQS data for HCHO and NO<sub>2</sub>  
173 from each site are only used for days in which both species are measured. Valid and continuous data points were then averaged to  
174 obtain seasonal summertime mean (JJA) values from 2005 to 2019 to be intercompared with corresponding OMI VCD values.

175 The AQS NO<sub>2</sub> data suffers from potential interference of reactive nitrogen species while measuring NO converted from  
176 NO<sub>2</sub> in molybdenum catalytic converters, since other reactive species also get converted to NO. We attempted to account for this  
177 interference by applying a model simulated correction factor (CF; Eq. 1) to the raw AQS data, following the approach of previous  
178 studies (Lamsal et al., 2008; 2010; Cooper et al., 2020).

$$179 \quad CF = \frac{NO_2}{NO_2 + (0.15 \times HNO_3) + (0.95 \times PAN) + \text{Alkyl Nitrates}} \quad (1)$$

180 The CF is calculated using the MERRA2-GMI simulated concentrations of NO<sub>2</sub>, HNO<sub>3</sub>, peroxyacetyl nitrate (PAN), and alkyl  
181 nitrates, and by applying an assumed effective conversion efficiency of 15% for HNO<sub>3</sub> and 95% for PAN (see Lamsal et al., 2010).  
182 The AQS's method to measure HCHO is affected by interference from species such as O<sub>3</sub> and NO<sub>2</sub> and since there is insufficient  
183 information to correct those interferences, here we use uncorrected AQS HCHO data.

### 184 2.3 Surface emissions of NO<sub>x</sub>

185 To compare the long-term evolution of FNRs with human-induced changes in precursor emissions (anthropogenic emissions of  
186 NO<sub>x</sub>), we used the most recent Community Emissions Data System (CEDS v\_2021\_04\_21) NO<sub>x</sub> bottom-up emission data set  
187 (McDuffie et al., 2020). As explained in the results section of this manuscript, we focus our analysis on trends in NO<sub>x</sub> emission  
188 instead of HCHO as it was determined that trends in NO<sub>2</sub> concentrations clearly drive the global trends in FNRs. The CEDS data  
189 provides monthly anthropogenic NO<sub>x</sub> emissions at  $0.5^\circ \times 0.5^\circ$  horizontal spatial scales from 1750–2019. For this study we analyse  
190 trends in anthropogenic NO<sub>x</sub> emissions (source sectors: Agriculture; 1: Energy; 2: Industrial; 3: Transportation; 4: Residential,

191 Commercial, Other; 5: Solvents production and application; 6: Waste; 7: International Shipping) between 2005 – 2019 to overlap  
192 with OMI observations. We used mean emissions for summer months (JJA) for each year to intercompare with OMI derived NO<sub>2</sub>  
193 and FNR trends. Since our focus in this study was to assess the overall relationship of long-term changes in OMI-derived FNR  
194 values and corresponding changes in the anthropogenic NO<sub>x</sub> over a city/region, we do not consider other natural sources (e.g.,  
195 biomass burning) contributing to ambient concentrations of urban NO<sub>2</sub>.

## 196 **2.4 Spatiotemporal analysis of FNRs**

197 The spatiotemporal analysis of OMI-derived VCD NO<sub>2</sub> and HCHO values was conducted as follows. First, summer-mean trends  
198 from 2005 to 2021 of HCHO and NO<sub>2</sub> VCDs and FNR values were calculated at the native spatial resolution (0.1° × 0.1°). Long-  
199 term trends were calculated for each grid of HCHO, NO<sub>2</sub>, and FNRs with ordinary least-squares linear regression (at various  
200 confidence levels calculated with the Mann-Kendall Test) similar to past studies (e.g., Boys, et al., 2014; Kharol et al., 2015;  
201 Geddes et al., 2016). To reduce retrieval random errors and improve precision, we focus on summer-mean data for each year and  
202 multi-year means (three multi-year means: 2005 – 2010, 2011 – 2015 and 2016 – 2021) around 46 cities across the Northern  
203 Hemisphere. The focus on the summer season was also chosen to utilize HCHO VCD retrievals with significantly better signal to  
204 noise ratios compared to winter, spring, and fall months. High levels of surface HCHO concentrations over source regions form  
205 due to the higher oxidant availability in summer (González Abad et al., 2015; Zhu et al., 2014; 2017a; 2017b) which leads to better  
206 retrievals of HCHO VCDs. We restrict our analysis to the Northern Hemisphere as most continental polluted regions exist there.  
207 We assessed the evolution of FNRs over urban and rural/suburban (hereinafter referred to just as rural) areas around cities. To  
208 define urban city regions, we used the hybrid dataset, CGLC-MODIS-LCZ (Demuzere et al., 2023), which is based on the  
209 Copernicus Global Land Service Land Cover (CGLC) product resampled to MODIS IGBP classes (CGLC-MODIS) and the global  
210 map of Local Climate Zones (LCZ) (Stewart and Oke., 2012) that describe the heterogeneous urban land surface. This data set was  
211 interpolated onto a 0.1° × 0.1° grid to match the resolution of the L3 OMI satellite data. Urban classification is defined by the  
212 CGLC-MODIS-LCZ land use categories 51 – 60, which includes a range of urban land use from sparsely built to compact high-rise  
213 including the heavy industry category. These land use categories capture both urban and suburban landscapes. Rural grids are those  
214 not defined as urban and within 7 × 7 grid boxes of the city center. The CGLC-MODIS-LCZ urban and rural maps derived for this  
215 study are static and will not capture urban expansion which has occurred over the last two decades. However, since our urban  
216 classification includes both urban and suburban landscapes (including sparsely built-up areas), the transition from suburban to  
217 urban landscapes will already be included in our urban map. The only thing not captured would be the transition from completely  
218 vegetative areas to more built-up landscapes which are expected to have a minor impact on the results of this study.

219 In this study, we focus only on the spatiotemporal variability of indicator ratios, rather than the exact ozone sensitivity  
220 regimes which can be inferred from these ratios. Although several previous studies assigned ratio values to certain O<sub>3</sub> regimes  
221 (e.g., Jin et al., 2017; Souri et al., 2017) based on previous modelling and limited-observational studies, large uncertainty exists in  
222 the classification of O<sub>3</sub> regimes using FNR values (Schroeder et al., 2017; Jin et al., 2020; Souri et al., 2021). Nevertheless,  
223 whenever the ratio values were assessed over a city/region, we also presented the threshold ratio values (separating O<sub>3</sub> regimes)  
224 suggested by Jin et al. (2020) for some cities in the US (Los Angeles, New York, Chicago, Washington DC, Pittsburgh, Atlanta  
225 and Houston), Wang et al. (2021) for cities in China, and Duncan et al. (2010) for all other cities/regions. Note that the threshold  
226 FNR values (< 1 as radical-limited versus > 2 as NO<sub>x</sub>-limited) suggested by Duncan et al. (2010) is a crude approximation as  
227 opposed to more recent and observationally-constrained threshold ratio values suggested by Jin et al. (2020) and Wang et al. (2021).  
228 We believe that an accurate classification of O<sub>3</sub> regimes is still an ongoing research topic (Schroeder et al., 2017; Jin et al., 2020;  
229 Souri et al., 2021) which should be addressed in future studies.

### 230 3. Results

#### 231 3.1 Long-term mean OMI data

232 Figure 1 shows the long-term mean (2005-2021) maps of OMI-derived VCDs of HCHO and NO<sub>2</sub> and the corresponding column  
233 FNR values. Formaldehyde enhancements reflect surface emissions of anthropogenic VOC (densely populated regions in China;  
234 Shen et al., 2019), biogenic isoprene (southeast US; Millet et al., 2008), and biomass burning (South Asia; Mahajan et al., 2015).  
235 OMI VCD NO<sub>2</sub> is abundant over urban areas primarily due to fossil fuel combustion emissions from traffic (Duncan et al., 2015)  
236 and over regions with large industrial activities (Krotkov et al., 2016). The column FNRs clearly reveal lower values over cities  
237 (FNR < 2), marginal values over rural/suburban regions surrounding large cities (FNR in the range of 2 - 5), and higher values  
238 elsewhere (FNR > 5). The lower FNRs over cities suggest radical-limited conditions, and larger FNR values in non-polluted  
239 background regions reflect NO<sub>x</sub>-limited conditions (Martin et al., 2004; Duncan et al., 2010; Jin et al., 2017; 2020; Wang et al.,  
240 2021). Lower FNR values retrieved by OMI are most noticeable in the highly populated regions of the US (e.g., Los Angeles, New  
241 York, Chicago), Europe (e.g., London, Amsterdam, Paris), East Asia (e.g., Beijing, Shanghai, Jinan), and Middle East (e.g., Dubai,  
242 Tehran, Riyadh) where tropospheric column NO<sub>2</sub> abundances are enhanced. The highest FNR values are observed in regions of  
243 the southeast US and south Asia (e.g., Malaysia) where there are no large cities and enhanced tropospheric column HCHO  
244 abundances, primarily from biogenic emissions, are observed.

#### 245 3.2 Capability of OMI VCD data to observe surface-level FNR trends

246 Before assessing VCD FNR trends, we compared trends in OMI NO<sub>2</sub> and HCHO VCD data, and corresponding tropospheric  
247 column FNRs, to surface in situ measurements from EPA AQS in the US in order to determine whether OMI VCD information  
248 tracks trends occurring at the surface. Figure 2 shows the 15-year time-series (2005-2019) comparison between normalized time  
249 series of OMI VCD indicator species abundances and FNRs and AQS data over select cities (US cities with continuous AQS data),  
250 and over all cities averaged across the continental US (USA, 373 separate sites). Table 1 shows the correlation between OMI VCD  
251 and AQS in situ NO<sub>2</sub>, HCHO, and FNR summer mean values in addition to the simple linear regression slope of normalized trends  
252 from OMI and AQS for both indicator species and FNRs. Figure 2 shows that both OMI VCD and in situ AQS data have relatively  
253 neutral trends in HCHO between 2005 and 2019 for most of the large urban cities of the US. While there is large interannual  
254 variability in HCHO concentrations, the long-term trends are relatively flat. On average, the normalized linear trends in surface  
255 HCHO in urban regions of the US was -0.05 yr<sup>-1</sup> and OMI VCDs was +0.15 yr<sup>-1</sup>. OMI VCD HCHO data is unable to replicate the  
256 interannual variability and long-term trends of surface data displayed by the low correlation values and opposing trends in multiple  
257 large cities in the US. The inability of OMI to reflect the variability in HCHO observed at the surface is likely due to the coarse  
258 spatial resolution of the OMI footprint, large noise in OMI HCHO retrievals (e.g., Johnson et al., 2023, Souri et al., 2023a), and  
259 complex vertical distributions of HCHO complicating satellite retrievals and representation of surface values (e.g., Souri et al.,  
260 2023b).

261 OMI VCD and in situ AQS data of NO<sub>2</sub> display a different story where statistically significant reductions at a 95%  
262 confidence level in NO<sub>2</sub> concentrations are observed by both data sources. The normalized trends in NO<sub>2</sub> from both measurement  
263 platforms are in strong agreement (see Fig. 2 and Table 1). Correlation between OMI VCD and AQS NO<sub>2</sub> was near 1.0 (R=0.98)  
264 and both data sources had normalized linear regression slopes of ~-0.20. This suggests that OMI is able to observe the strong  
265 reduction in NO<sub>2</sub> concentrations at the surface measured by AQS across the US. Both data sources suggest that NO<sub>2</sub> reduced  
266 between 2005-2019 and the strongest negative trends were in the large cities of the US such as New York, Chicago, and Los  
267 Angeles. The near neutral trend in HCHO and large decreases in NO<sub>2</sub> results in both OMI VCD and in situ data sources observing

268 an increasing trend in FNR data in all major cities of the US shown in Fig. 2. The normalized linear regression trend slopes of  
269 FNRs (0.21 from both OMI and AQS data) are all statistically significant reductions at a 95% confidence level and are nearly equal  
270 and opposite to NO<sub>2</sub>, suggesting the reduction of NO<sub>2</sub> is the primary driver of FNR trends over time. It is encouraging that OMI  
271 VCD data is able to accurately reproduce the normalized trends in surface FNRs in the US. This agrees with the recent studies  
272 from Jin et al. (2017) and Souri et al. (2023a) which show that ratios of mid-day tropospheric VCD FNRs to PBL and surface-  
273 level concentrations are near unity. Since OMI VCD FNRs appear to be able to replicate the trends in surface FNRs, the rest of  
274 this study focuses on the trends of FNRs from OMI VCD data for the Northern Hemisphere.

### 275 3.3 17-year trend in OMI observations

276 This study investigates the 17-year trend of OMI VCD of HCHO, NO<sub>2</sub> and FNR values between 2005 and 2021. Figure 3 shows  
277 the long-term trend in OMI VCD HCHO, NO<sub>2</sub> and FNR values at an 85% confidence level ( $p \leq 0.15$ ) (Fig. S1 shows the same  
278 trend values at a 99% [ $p \leq 0.01$ ] confidence level and for all grid cells with OMI retrievals). The same information shown in Fig.  
279 3 is displayed individually for North America, Europe, and Asia in the supplemental information (see Fig. S2). Formaldehyde  
280 VCDs increased by  $\sim 0.5 \times 10^{14}$  molecules cm<sup>-2</sup> yr<sup>-1</sup> over most of the Northern Hemisphere, with reductions up to  $\sim 0.5 \times 10^{14}$   
281 molecules cm<sup>-2</sup> yr<sup>-1</sup> over the southeast US. This trend is consistent with previous studies documenting increases in multi-satellite  
282 (including OMI) summer mean HCHO over Northern China (during 2005-2016 [Shen et al., 2019] and 2005-2014 [Souri et al.,  
283 2017]) and increases in most regions in the US (during 2005-2014 [Zhu et al., 2017b]) due to increasing anthropogenic VOC  
284 emissions. Some near neutral trends, to small decreases, are seen in Fig. 3 in eastern China. The decrease in HCHO over Southern  
285 China could be due to reductions in anthropogenic VOCs (Souri et al., 2017; Itahashi et al., 2022) or biogenic VOC emissions as  
286 noted by Jin and Holloway (2015). The decreases in summer mean OMI HCHO over the southeast US were also documented in  
287 earlier studies (De Smedt et al. 2015; Zhu et al., 2017b). Note that the trend in HCHO calculated in this study is influenced by  
288 yearly variations in temperature, in contrast to Shen et al. (2019) and Zhu et al. (2017b) that corrected for the impact of varying  
289 temperature on HCHO VCDs.

290 It should be noted that the NASA-released operational OMI HCHO version 3 collection 3 data product used in this study  
291 has been shown to have a positive drift due to instrument aging (e.g., Marais et al., 2012; Zhu et al., 2014, 2017b). This positive  
292 trend in OMI HCHO data displayed in Fig. 3 is likely largely impacted by the artificial positive drift in the collection 3 OMI data.  
293 A new NASA OMI HCHO version 3 collection 4 product is in development using the SAO algorithm which has removed this  
294 positive drift in HCHO (Ayazpour et al., 2024; personal communication with the SAO HCHO algorithm team). This new HCHO  
295 retrieval product shows that HCHO has a near-neutral trend across most of the populated cities in the Northern Hemisphere. This  
296 new collection 4 retrieval data is not yet peer-reviewed or available to the public therefore is not used here and the remaining  
297 results in this study use OMI HCHO version 3 collection 3 data. However, to test the potential impact on the results of this study  
298 using an OMI VCD product with this average positive drift eliminated, we removed the mean annual Northern Hemispheric HCHO  
299 trend ( $\sim 0.004$  DU yr<sup>-1</sup>) from the collection 3 data and evaluate the resulting FNR trends over 18 selected large cities in the Northern  
300 Hemisphere which is discussed in Sect. 3.4.

301 The negative trend in NO<sub>2</sub> OMI VCDs over populated regions of the US, Europe, and eastern China, and increases in the  
302 South Asia and Middle East regions, seen in Fig. 3 are consistent with several previous studies (e.g., Hilboll et al., 2013; Jin et al.,  
303 2017). The decreases in eastern China and Europe are as large as  $-2.0 \times 10^{14}$  molecules cm<sup>-2</sup> yr<sup>-1</sup> while reductions in NO<sub>2</sub> in the  
304 US are between  $-0.1$  to  $-1.0 \times 10^{14}$  molecules cm<sup>-2</sup> yr<sup>-1</sup>. The decreasing NO<sub>2</sub> trend in eastern China could be due to recent reductions  
305 in anthropogenic NO<sub>x</sub> emissions after year 2011 (e.g., Fan et al., 2021). It is well demonstrated that the tropospheric NO<sub>2</sub> decreases  
306 in most Northern Hemisphere regions, particularly in urban regions, is due to reductions in anthropogenic NO<sub>x</sub> emissions



307 implemented through national governmental policies (e.g., Duncan et al., 2016; Koplitz et al., 2021). Figure S3 shows the trends  
308 in CEDS anthropogenic NO<sub>x</sub> emissions between 2005-2019 which have nearly identical regions of reduction as those retrieved by  
309 OMI NO<sub>2</sub>. Overall, the summer-mean trend in VCD NO<sub>2</sub> estimated in this study is generally consistent with the reported satellite-  
310 based annual mean surface NO<sub>2</sub> trend estimated on a global-scale (Geddes et al., 2015) and over the US (Kharol et al., 2015;  
311 Lamsal et al., 2015).

312 The most notable feature in Fig. 3 is the general increasing trend in OMI VCD FNR values over most of the polluted  
313 regions in the Northern Hemisphere. The increasing OMI column FNR values suggest a trend towards more NO<sub>x</sub>-limited regimes  
314 around cities in recent years which has been noted by some previous studies (Jin et al., 2017; 2020; Souri et al., 2017). Increases  
315 in FNRs in the populated regions of China, Europe, and US reach values between 0.1 and 0.2 yr<sup>-1</sup>. The increases in FNRs are  
316 driven mostly by the reductions in NO<sub>2</sub> rather than the small variations in HCHO, as evident in Fig. 2 and 3. The following sections  
317 focus on the assessment of the evolution of summer mean OMI-derived VCD FNRs over numerous selected cities in the Northern  
318 Hemisphere.

### 319 **3.4 Evolution of OMI FNRs around populated cities in the Northern Hemisphere**

320 Figure 4 shows the time series of summer mean OMI VCD FNRs from 2005 to 2021 over 18 selected large cities. The  
321 corresponding normalized time series trends of OMI-derived NO<sub>2</sub> abundances and FNRs, and CEDS anthropogenic emissions of  
322 NO<sub>x</sub> over these cities, are displayed in Fig. 5. From Fig. 4 it can be seen that the largest positive trends in OMI FNRs during the  
323 2005-2021 time period occurred over three mega-cities in the US: Los Angeles, New York and Chicago. Time series of the actual  
324 magnitudes of OMI VCD NO<sub>2</sub> and HCHO abundances over the selected 18 large cities are shown in Fig. S4. In addition to increases  
325 in FNRs in US cities, relatively large increases in FNRs are also evident in European (e.g., London) and Asian (e.g., Guangzhou)  
326 cities. To test whether the positive drift in the NASA OMI HCHO collection 3 data significantly impacted the results of the FNR  
327 trends over the 18 selected large cities in the Northern Hemisphere we present these same results in Fig. S5 with the OMI data  
328 which has the annual average Northern Hemispheric HCHO trend removed (more representative of OMI HCHO version 3 collection  
329 4 data) and Fig. S6 shows the spatial trends of HCHO, NO<sub>2</sub>, and FNRs over the Northern Hemisphere using this detrended HCHO  
330 data. Comparing Figs. S5 and 4, it is seen that while some of the FNR values are slightly lower in magnitude the positive trends  
331 are very similar using collection 3 HCHO retrievals and a data product with the positive drift removed. Throughout the Northern  
332 Hemisphere HCHO trends now display both positive and negative values (see Fig S6) instead of the constant positive trends from  
333 the OMI HCHO collection 3 product. Using the detrended OMI HCHO data does result in more negative FNR trends in remote  
334 regions outside of large urban regions; however, over urban areas, and rural regions surrounding large cities, the FNR trends are  
335 still positive as displayed in Fig. S5 and S6. Overall, using the OMI HCHO version 3 collection 3 data product does not significantly  
336 impact the FNR results in large cities in the Northern Hemisphere focused on in this study. Future studies investigating FNRs  
337 conducted when the NASA OMI HCHO version 3 collection 4 data is available to the public should however use this new product  
338 to present more accurate results compared to those shown here using the NASA OMI HCHO version 3 collection 3 product.

339 Figure 5 reveals that the increases in OMI FNR values over the selected 18 mega-cities are linked with decreases in NO<sub>2</sub>  
340 abundances due to reductions in anthropogenic NO<sub>x</sub> emissions. The spatial map of trends in CEDS anthropogenic emissions of NO<sub>x</sub>  
341 across the Northern Hemisphere between 2005-2019 are shown in Fig. S3 (timeseries of CEDS NO<sub>x</sub> emission magnitudes for the  
342 selected 18 mega-cities shown in Fig. S7). Based on the O<sub>3</sub> production sensitivity regime thresholds suggested by Jin et al. (2020)  
343 (note that these thresholds are applicable for VCD data), all the US cities shown in Fig. 4 that were VOC-limited in the early 2000's  
344 show clear transition towards NO<sub>x</sub>-limited and transitional regimes in recent years. Major cities in Europe such as London and  
345 Amsterdam have also experienced increasing FNRs moving from VOC-limited regimes to transitional, or even NO<sub>x</sub>-limited,

346 regimes in recent years (based on thresholds from Duncan et al. [2010]). Increases in the magnitudes of FNRs were generally  
347 smaller in large cities of Asia; however, only Neijiang doesn't display some noticeable increases in FNRs in recent years. In  
348 Neijiang, CEDS anthropogenic NO<sub>x</sub> emissions are decreasing after 2012; however, OMI does not retrieve decreasing NO<sub>2</sub>  
349 abundances leading to the near-neutral trend in FNR values. Based on the O<sub>3</sub> production sensitivity regimes thresholds defined by  
350 Wang et al. (2021) and Duncan et al. (2010), major cities in Asia have FNR values which are in the transitional or NO<sub>x</sub>-limited  
351 regimes in recent years besides Beijing, Shanghai, Jinan, and Riyadh (surrounding rural region is in the transitional regimes) (see  
352 Fig. 4). Figure 5 shows these large Asian cities, besides Riyadh, implemented NO<sub>x</sub> emission control strategies in ~2012 and have  
353 recent negative trends in OMI NO<sub>2</sub>; however, based on Wang et al. (2021) these urban regions have O<sub>3</sub> production which is still  
354 limited by VOCs. Overall, it is difficult to conclude if these major cities in the Northern Hemisphere have in fact transitioned to  
355 NO<sub>x</sub>-limited and transitional regimes due to the large uncertainties in the exact threshold FNR values which separate these chemical  
356 regimes.

357 In the vast majority of cities between 2005-2021 OMI retrieved larger FNR values in the rural regions surrounding urban  
358 regions in the Northern Hemisphere compared to the urban city centers. Figure 6 shows spatial maps of OMI-derived VCD FNRs  
359 around the selected 18 cities discussed above for two 6-year averages: 2005-2010 and 2015-2021 reflecting the earliest and most  
360 recent years of OMI data studied here. The spatial maps of OMI-derived HCHO and NO<sub>2</sub> VCD values for these same time periods  
361 over the 18 cities are displayed in Fig. S8 and S9, respectively. Figure 6 shows that OMI is able to retrieve the differences in FNRs  
362 in urban and rural regions surrounding large cities in the Northern Hemisphere (Fig. S10 shows the same information in Fig. 6  
363 except with the CGLC-MODIS-LCZ urban grids used to separate urban and rural values). In urban areas of cities, where emission  
364 sources of NO<sub>x</sub> are largest, OMI FNRs tend to be lower indicating more tendency towards VOC-sensitive O<sub>3</sub> production regimes  
365 compared to the surrounding rural regions. This figure also displays the decadal-scale changes (2016–2021 versus 2005–2010) in  
366 the OMI FNRs over the Northern Hemisphere urban regions and surrounding rural regions. In all 18 cities FNR values increase in  
367 both rural and urban areas with noticeable increases in the spatial coverage of potentially NO<sub>x</sub>-limited O<sub>3</sub> production regimes.  
368 These spatial distributions of increasing FNR values retrieved by OMI are clearly correlated with decreasing tropospheric NO<sub>2</sub>  
369 over the vast majority of cities displayed in Fig. S9. Large cities in the US show the clearest increase in the spatial coverage of  
370 potentially NO<sub>x</sub>-limited O<sub>3</sub> production regimes; however, European and Asian cities also follow a similar pattern with less increase  
371 in FNR magnitude overall. Recent studies have also noted that NO<sub>x</sub>-limited regimes have expanded spatially into the city centers,  
372 on a decadal-scale, throughout the Northern Hemisphere (Jin et al., 2017) and in the US (Jin et al., 2020). This has large implications  
373 for O<sub>3</sub> sensitivity analysis and development of future emission control strategies for improving air quality.

374 Figure 7 shows the changes in OMI FNRs (multi-year averaged values: 2005-2010, 2011-2015, and 2016-2021) over 46  
375 cities in the Northern Hemisphere. The vast majority of urban regions in the Northern Hemisphere (44 of the 46 selected cities)  
376 experienced increasing FNRs between 2005-2010 and 2016-2021. OMI FNRs for Tehran, Iran and Neijiang, China were two  
377 selected cities which did not display increasing values. On average, FNRs in urban areas of the selected cities increased by ~65%  
378 between 2005-2010 and 2016-2021. Similar to urban regions, the vast majority of rural regions surrounding urban areas in the  
379 Northern Hemisphere (44 of the 46 selected cities) experienced increasing FNRs between 2005-2010 and 2016-2021. The average  
380 increase of FNRs in the rural regions increased slightly less (~38%) compared to urban areas. In agreement with results discussed  
381 above, FNR values in rural regions are larger compared to city centers. However, OMI VCD FNR differences between rural and  
382 urban regions were reduced by ~15% on average over the 17-year time period. This suggests that the urban/rural interface of FNRs  
383 is becoming less drastic and NO<sub>x</sub>-limited O<sub>3</sub> production regimes that in the past were predominantly observed in rural regions have  
384 expanded into the urban regions of larger cities. More accurate assessment of the actual threshold ratio values separating the  
385 different O<sub>3</sub> production regimes would allow for the determination of exactly what extent of each city has in fact transitioned to

386 NO<sub>x</sub>-limited regimes. Overall, Fig. 7 demonstrates that the long-term record of OMI observations can observe the impact of global  
387 emissions reduction strategies on air quality and O<sub>3</sub> sensitivity regimes throughout the Northern Hemisphere.

### 388 **3.5 Impact of the COVID-lockdown on FNRs in the Northern Hemisphere**

389 The global impacts of the COVID-lockdown in 2020 on atmospheric pollution, such as the reduction of tropospheric NO<sub>2</sub>, has  
390 been well documented to have impacted O<sub>3</sub> sensitivity regimes in the PBL and mid- to upper-troposphere (e.g., Goldberg et al.,  
391 2020; He et al., 2020, Cooper et al., 2022; Nussbaumer et al., 2022). Here we studied, for the first time, OMI derived VCD FNRs  
392 to evaluate the impact of the COVID-lockdown on summer-mean FNRs in 2020 throughout the Northern Hemisphere compared  
393 to the year before (2019) and after (2021). Figure 8 shows the changes in OMI FNRs before, during, and after (2019, 2020, 2021)  
394 the COVID-lockdown over the selected 46 cities discussed in this study. Out of the 46 selected cities, 32 of the urban regions  
395 (~70%) experienced higher FNRs in 2020 compared to 2019. On average, the cities that experienced increased FNRs in 2020 had  
396 values which were ~19% higher compared to 2019. Similarly, 26 of the urban regions (~57%) experienced higher FNRs in 2020  
397 compared to 2021 and these city centers had FNR values ~18% larger. OMI also retrieved increased FNR values in rural regions  
398 surrounding city centers throughout the Northern Hemisphere during the COVID-lockdown period of 2020 (see Fig. 8). A similar  
399 number of city's rural areas experienced increased FNRs in 2020 compared to 2019 and 2021 as what was observed for urban  
400 areas. The increases in FNRs for rural regions in 2020 compared to 2019 and 2021 were 16% and 13%. The OMI data evaluated  
401 here suggest that the majority of cities in the Northern Hemisphere, and surrounding rural regions, tended to have O<sub>3</sub> production  
402 which was more sensitivity to NO<sub>x</sub> emissions/concentrations in 2020 compared to the year before and after. Cooper et al. (2022)  
403 demonstrated that in 2020 NO<sub>2</sub> concentrations were on average ~30% lower during COVID-lockdown periods and these reductions  
404 were from decreased anthropogenic emissions and can't be explained by meteorological differences. The degree of reduction in  
405 NO<sub>2</sub> determined in Cooper et al. (2022) agrees well with the OMI VCD FNR increases determined during our study of ~20%.

### 406 **3.6 Comparison of OMI and TROPOMI FNR spatiotemporal variability in US cities**

407 To expand upon previous studies which investigated OMI FNR trends published prior to the availability of TROPOMI retrievals  
408 (e.g., Mahajan et al., 2015; Jin and Holloway, 2015; Sourì et al., 2017; Jin et al., 2017, 2020), here we compare the ability of OMI  
409 and TROPOMI to reproduced inter-city and interannual FNR variability in the US measured by EPA AQS sites in the 7 major US  
410 cities illustrated in Fig. 2. For this purpose, we applied TROPOMI L2 HCHO version 2.1 and NO<sub>2</sub> version 3.6.2 interpolated to a  
411 standardized 0.1° × 0.1° grid format. Figure 9 shows the normalized summer mean FNRs (city-specific annual FNR values  
412 normalized by the 7-city FNR mean) for the 7 selected US cities for 2018 and 2019. For both years, TROPOMI was able to  
413 reproduce the inter-city variability in normalized FNRs more accurately compared to OMI for 5 of the 7 US cities. This is further  
414 emphasized by the fact that TROPOMI reproduced 48% and 93% of the inter-city FNR variance (R<sup>2</sup>) measured by AQS data for  
415 2018 and 2019, respectively, while OMI only reproduced ~30% of the FNR variability measured in both years. Furthermore,  
416 TROPOMI accurately reproduced the direction of change in AQS measured FNRs between 2018 and 2019 for 6 of the 7 cities  
417 (85%) while OMI was only able to reproduce the FNR differences for 3 of the 7 cities (43%). The improved capability of  
418 TROPOMI to capture spatiotemporal FNR variability compared to OMI is to be expected as recent studies have demonstrated  
419 improved HCHO and NO<sub>2</sub> retrievals from the newer and higher spatial resolution sensor (e.g., Sourì et al., 2023a; Johnson et al.,  
420 2023) and OMI is far past the expected lifetime of the sensor. Future studies should intercompare the two sensor's retrievals of  
421 FNRs for the entire lifetime of TROPOMI which overlaps with OMI (2017-present) to fully understand the improvements when  
422 applying TROPOMI.

#### 423 4. Discussing the use of OMI data to assess O<sub>3</sub> production sensitivity regimes

424 The OMI satellite sensor offers a continuous data record across the globe with sufficient spatiotemporal resolution to assess  
425 tropospheric O<sub>3</sub> production sensitivity which cannot be achieved with in situ observations. The analysis in this study demonstrated  
426 that the 17-year record of OMI-retrieved HCHO and NO<sub>2</sub> data offered an unprecedented opportunity to assess the long-term  
427 evolution of VCD, and likely surface-level, FNR values, with potential future applications in linking these ratio changes with  
428 changes in surface O<sub>3</sub> regimes. Here we show that OMI VCD data of FNRs replicate the trends observed with surface in situ  
429 information. In order to produce actual satellite-derived surface values of HCHO, NO<sub>2</sub>, and FNRs using VCD retrievals requires  
430 algorithms which largely depend on CTM-predicted vertical distributions of these trace gases (e.g. Zhu et al., 2017a; Jin et al.,  
431 2017; Cooper et al., 2020). Surface-based and aircraft in situ observations are also used for this purpose; however, these  
432 observations have minimal observational coverage due to being very spatiotemporally limited (e.g., Souri et al., 2023a). Using  
433 model simulations or in situ data to convert satellite VCD information to surface-level HCHO, NO<sub>2</sub>, and FNRs concentrations are  
434 both inhibited by errors. In situ observations are too sparse and CTMs have system-specific errors/biases and differ largely in their  
435 prediction of HCHO and NO<sub>2</sub> vertical distributions (Lamsal et al., 2008; Geddes et al., 2016; Souri et al., 2023b). This results in  
436 large uncertainties in surface-level FNRs when convolving satellite VCDs. Our study does not address the conversion of OMI  
437 VCDs to surface-level values, but clearly shows that this spaceborne sensor can capture the trends in surface-level FNRs. The  
438 ability of VCD information from low earth orbit satellites to capture mid-day surface-level FNR trends might be due to studies  
439 showing ratios of VCD FNRs to PBL/surface values are near unity (Jin et al., 2017; Souri et al., 2023a). However, during times  
440 where HCHO and NO<sub>2</sub> vertical profiles in the troposphere are not similar to climatological averages, models and satellites may be  
441 challenged to accurately assess conversion ratios of VCD FNRs to PBL/surface values (e.g., Souri et al., 2023b). Overall, if  
442 methods are improved to reduce the uncertainty in the conversion of satellite VCD retrievals of HCHO and NO<sub>2</sub> to surface-level  
443 concentrations, then satellite-derived surface-level FNRs will be able to be applied in higher confidence for air quality research  
444 and potentially policy decisions.

445 OMI VCD FNR and NO<sub>2</sub> retrievals display high correlation with surface in situ data trends (see Table 1). However, this  
446 satellite demonstrated less capability to replicate trends of surface-level observations of HCHO. The vertical structure of HCHO  
447 can be complex which complicates the relationship between VCDs and surface-level values (Souri et al., 2023b); however, OMI  
448 has also been shown to have large systematic and random biases in HCHO retrievals which drive the overall errors in OMI-derived  
449 VCD FNRs (Johnson et al., 2023; Souri et al., 2023a). However, since decreasing NO<sub>2</sub> emissions/concentrations driven by NO<sub>x</sub>  
450 emission control strategies is the primary reason for the increasing trends of FNRs at the surface, while HCHO has near-neutral  
451 trends, and OMI NO<sub>2</sub> VCDs have much lower errors compared to HCHO (Johnson et al., 2023; Souri et al., 2023a), this study  
452 shows that OMI VCD data of indicator species can still replicate surface-level trends of FNRs. Emission control strategies for  
453 VOCs have also been shown to have caused regional reductions in the concentrations of these compounds; however, it is  
454 challenging to derive and assess the impact of VOC emission control strategies as there are thousands of different VOC compounds  
455 all with different chemical reactivity (Pei et al., 2022). Furthermore, a large fraction of VOCs is emitted from biogenic sources  
456 which cannot be controlled through changes in human activities (Guenther et al., 1995). In addition to retrieval errors, the coarse  
457 spatial resolution of OMI and other spaceborne sensors results in representation errors when compared to point-source surface  
458 observations (Souri et al., 2022). This also likely contributes to the challenge of satellite-derived HCHO, NO<sub>2</sub>, and FNRs to  
459 replicate trends and variability determined from in situ measurements located in city centers.

460 Besides the southeast US and some small areas of eastern China, OMI HCHO version 3 collection 3 data results in mostly  
461 positive trends between 2005-2021. A portion of this positive trend could be due to the OMI instrument drift which has been  
462 identified in past studies (e.g., Marais et al., 2012; Zhu et al., 2016, 2017b). Currently, there is an OMI HCHO version 3 collection

463 4 product in development using the SAO algorithm; however, has yet to be published and therefore could not be applied in this  
464 study. A major difference between the collection 3 and 4 data products is how level 1b (L1b) data is produced as described in  
465 Kleipool et al. (2022). Furthermore, changes in molecular absorption cross-sections and input parameters for SCD calculations,  
466 AMF calculations, and latitudinal bias corrections are applied in collection 4 OMI HCHO data. Preliminary analysis of the  
467 differences in OMI VCD HCHO using the collection 3 and 4 data demonstrates changes in the magnitudes and trends of this  
468 species (personal communication with the SAO OMI HCHO algorithm team). These differences could have an impact on the  
469 analysis of trends in global FNRs such as that conducted in this study. Once the OMI HCHO version 3 collection 4 product becomes  
470 available to the public the analysis in this study should be redone with the updated HCHO data. Overall, we don't expect that the  
471 results in FNR trends will be impacted much due to observed trends in OMI VCD and surface-level NO<sub>2</sub> being much larger than  
472 that in HCHO (see Sect. 3.2).

473 Due to the inadequacy of our current quantitative understanding of exact threshold FNR values marking the O<sub>3</sub>  
474 photochemical regime transitions (e.g., Schroeder et al., 2017), this study avoided explicitly linking OMI FNRs with exact chemical  
475 regimes. An accurate diagnosis of surface O<sub>3</sub> sensitivity requires more in-depth analysis of satellite FNRs at a higher spatiotemporal  
476 resolution, and accurately relating these FNRs to O<sub>3</sub> regimes by estimating the threshold ratio values applicable to specific regions  
477 and time periods. Global CTM simulations (Jin et al., 2017), photochemical box modeling utilizing measurement data from  
478 airborne field campaigns (Schroeder et al., 2017; Souri et al., 2020), and observation-based methods linking ratio values with  
479 surface O<sub>3</sub> concentrations (Jin et al., 2020; Wang et al., 2021) could lead to the derivation of more accurate regime threshold ratio  
480 values. Nevertheless, the OMI-derived VCD FNR values investigated in this study revealed many aspects of O<sub>3</sub> sensitivity to NO<sub>x</sub>  
481 versus VOCs. In general, OMI-derived summer FNR values indicated radical limited regimes within many cities in the Northern  
482 Hemisphere (FNRs < 2) and NO<sub>x</sub>-limited regimes over the rural regions around those cities (FNRs > 3). The analysis of multi-year  
483 summer mean OMI HCHO and NO<sub>2</sub> values revealed a positive trend in FNRs indicating a transition from radical-limited to NO<sub>x</sub>-  
484 limited regimes, especially during more recent years. The positive trend in OMI FNRs over most cities are mainly due to decreases  
485 in NO<sub>2</sub> resulting from the decrease in anthropogenic NO<sub>x</sub> emissions and mixed-variations in biogenic VOC sources. This study  
486 evaluated FNR trends for 46 large Northern Hemisphere cities which expands on other recent studies which evaluated O<sub>3</sub>  
487 production sensitivity regimes around smaller numbers of cities (e.g., Jin et al., 2017). Due to the majority of highly-populated  
488 Northern Hemisphere cities, outside of the Tropics, residing in developed nations, the increasing trend in FNRs due to  
489 anthropogenic emissions reductions holds true for the vast majority of the 46 cities studied here.

490 In the earliest years of studying satellite-derived FNRs it was hoped this data source could potentially be used for policy  
491 decisions and developing emission control strategies (Martin et al., 2004). However, more recent studies starting with Duncan et  
492 al. (2010) suggested that satellite retrievals may have errors too large for applying FNRs for air quality regulations. Furthermore,  
493 satellite data typically has to be temporally averaged to reduce noise in the retrievals which may mask out important O<sub>3</sub> exceedance  
494 events and the indicator species characteristics on these days (Schroeder et al., 2017). The recent study by Souri et al. (2023a)  
495 compiled a comprehensive error budget for using satellite retrievals to assess surface-level FNRs. This study showed that total  
496 relative error in satellite FNRs over large cities tend to be ~50% whereas over rural regions there are much larger errors (>100%).  
497 The majority of this error comes from noise in satellite retrievals (40%-90%), especially from HCHO retrievals, and the rest of  
498 this error is associated with the ability of indicator species to accurately describe complex O<sub>3</sub> chemistry (~20%), VCD to surface  
499 translation (~19%), and spatial representation (~13%). These total relative errors are likely too large to apply satellite FNRs for air  
500 quality regulation purposes; however, still provide a useful scientific research product for investigating long-term, and short-term  
501 events (e.g., meteorological variations, droughts/floods, wildfires, socioeconomic events, etc.), impacts of emissions on O<sub>3</sub>  
502 production sensitivity regimes.

#### 503 4 Conclusions

504 This study applied the 17-year data record of OMI satellite sensor's summer mean VCD HCHO, NO<sub>2</sub>, and FNRs between 2005  
505 and 2021 over the Northern Hemisphere to understand the long-term evolution of O<sub>3</sub> photochemical regimes. This expands the  
506 global OMI record of VCD FNRs out to 2021 further than previous studies (e.g., Jin et al., 2020). The long-term trends for 46  
507 highly populated cities in the Northern Hemisphere agree with past work which have shown that FNRs are primarily increasing  
508 due to reductions in emissions/concentrations of NO<sub>x</sub> (Duncan et al., 2010; Jin et al., 2017, 2020). OMI VCD NO<sub>2</sub> data are  
509 decreasing in most urban regions of the Northern Hemisphere, while HCHO data is near-neutral or slightly increasing, resulting in  
510 the increasing FNR trends. The extension of OMI FNR data out to 2021 suggests a continuing trend towards more NO<sub>x</sub>-limited O<sub>3</sub>  
511 production sensitivity regimes within and around cities throughout the Northern Hemisphere.

512 Another unique finding in our study is the extension of OMI FNR data out to 2021 covering the impact of the COVID-  
513 19 lockdown of 2020. Out of the 46 selected cities, ~70% of urban regions experienced higher FNRs in 2020 compared to 2019  
514 and ~57% had higher FNRs in 2020 compared to 2021. OMI FNRs were 18%-19% higher in 2020 compared to the year before  
515 and after the COVID-lockdown in 2020. We studied summer-mean FNRs in this study; however, COVID-lockdown restrictions  
516 were largest in the spring of 2020, thus the full impact of COVID-lockdown restrictions on VCD FNRs was likely larger than that  
517 experienced in the summer. A similar percentage of rural areas around the 46 selected cities experience higher FNRs in 2020  
518 compared to 2019 and 2021; however, the increases in FNRs were smaller (13%-16%) compared to urban areas. The OMI data  
519 evaluated here suggests that the majority of cities in the Northern Hemisphere, and surrounding rural regions, tended to have O<sub>3</sub>  
520 production which was more sensitive to NO<sub>x</sub> emissions/concentrations in 2020 compared to the year before and after.

521 Past studies have shown that mid-day FNR VCDs are similar to those observed at the surface (Jin et al., 2017; Souri et  
522 al., 2023a). However, during times where HCHO and NO<sub>2</sub> vertical profiles in the troposphere are complex, models and satellites  
523 may be challenged to accurately assess conversion ratios of VCD FNRs to PBL/surface values (e.g., Souri et al., 2023b). This  
524 study shows that on average the long-term trends of OMI VCD FNRs agree well with in observations at the surface in cities  
525 distributed around the US, suggesting that this satellite is capable to assess the long-term trends of surface-level O<sub>3</sub> production  
526 sensitivity regimes. However, the magnitudes of both indicator species calculated with satellite VCDs using scaling factors derived  
527 with CTMs and/or in situ observations are highly uncertain. Both OMI VCD and surface in situ data of HCHO, NO<sub>2</sub>, and FNRs  
528 emphasize that the increasing trend in FNRs is driven by reduced emissions/concentrations of NO<sub>2</sub> while HCHO has a near-neutral  
529 trend. While OMI VCD HCHO trends and variability do not agree well with surface in situ observations; OMI does replicate the  
530 strong decreasing trend of NO<sub>2</sub> observed at the surface resulting in the agreement between OMI and surface data of FNR trends.

531 Higher spatiotemporal retrievals from newer low earth orbit (e.g., TROPOMI) and geostationary (e.g., Tropospheric  
532 Emissions: Monitoring of Pollution [TEMPO], Geostationary Environment Monitoring Spectrometer [GEMS]) satellite sensors  
533 provide more insight into the short-term (daily, diurnal) recent (2017-present) evolution of O<sub>3</sub> photochemical regimes. Compared  
534 to OMI, TROPOMI was shown to retrieve VCD FNR values with more accuracy and better precision compared to OMI  
535 observations primarily due to improvements in HCHO product performance (e.g., Johnson et al., 2023). Johnson et al. (2023)  
536 demonstrated that TROPOMI can retrieve spatiotemporal HCHO variability with uncertainties low enough to capture FNR  
537 variability on a daily basis, while OMI was not. The current study compared the capability of OMI and TROPOMI to capture inter-  
538 city and interannual FNR variability measured by ground-based AQS data (using normalized FNR values) for 7 select US cities.  
539 Here we quantitatively showed that TROPOMI was able to reproduce the spatiotemporal variability in observed FNRs more  
540 accurately compared to OMI for the reasons mentioned above. Future improvements in satellite HCHO retrievals will allow for  
541 more accurate retrievals of FNRs on a daily- to monthly-scale. TEMPO and GEMS provide HCHO and NO<sub>2</sub> VCD information at  
542 1- to 3-hour temporal resolution and higher spatial resolution compared to both OMI and TROPOMI which will allow for the

543 assessment of diurnal FNR variability on a regional scale. This has not yet been possible as TEMPO and GEMS are the first  
544 UV/VIS spectrometers on geostationary platforms with spatial resolution high enough to retrieve air quality relevant HCHO and  
545 NO<sub>2</sub> VCD data. The new diurnal and high spatial resolution information from these geostationary satellites are expected to greatly  
546 improve the understanding of FNRs. As OMI is set to be decommissioned in the coming years, it is critical to merge TROPOMI  
547 HCHO and NO<sub>2</sub> VCD data with OMI in order to continue the long-term data set from 2005-present. Furthermore, combining  
548 retrieved information from geostationary satellites with once-a-day low earth orbit data will provide a vast wealth of information  
549 about global daily to hourly variability in FNRs.

550 While recent studies have shown that OMI FNR retrieval errors are likely too large to apply in air quality regulation and  
551 for deriving emission control strategies to reduce surface-level O<sub>3</sub> concentrations, this long-term satellite product provides a useful  
552 scientific research product for investigating atmospheric O<sub>3</sub> chemistry and investigating qualitative impacts of emission changes  
553 on O<sub>3</sub> production sensitivity regimes. This is especially true for regions of the globe outside of the US and Europe that have limited  
554 long-term surface in situ observation networks able to measure HCHO and NO<sub>2</sub> concentrations. Improvements in HCHO and NO<sub>2</sub>  
555 VCD retrieval algorithms and methods to derive VCD to surface/PBL conversion factors for these indicator species would greatly  
556 improve the ability to apply OMI and other satellite products to study surface air quality. Data assimilation and inverse models  
557 have been combined with satellite retrievals of HCHO and NO<sub>2</sub> data to constrain predictions of NO<sub>x</sub> and VOC emissions and  
558 resulting O<sub>3</sub> chemistry (e.g., Souri et al., 2020). These satellite data-constrained models can then be used to assess trends and  
559 variability in FNRs, indicator species emissions, and O<sub>3</sub> photochemistry regimes. These improvements in satellite retrieval  
560 algorithms, CTMs, data assimilation and inverse modeling techniques, along with studies to better define the actual O<sub>3</sub> production  
561 sensitivity regime thresholds, will allow for a more confident investigation of long-term air quality and the impacts of NO<sub>x</sub> and  
562 VOC emission changes on O<sub>3</sub> production sensitivity.

563 *Code and Data Availability.* The OMI HCHO L3 data used in this paper is publicly available at  
564 [https://acdisc.gesdisc.eosdis.nasa.gov/data//Aura\\_OMI\\_Level3/OMHCHOd.003/](https://acdisc.gesdisc.eosdis.nasa.gov/data//Aura_OMI_Level3/OMHCHOd.003/) (last access: 24 October 2021). The OMI NO<sub>2</sub>  
565 High Resolution L3 data is also available at a public data repository:  
566 [https://avdc.gsfc.nasa.gov/pub/data/satellite/Aura/OMI/V03/L3/OMNO2d\\_HR/OMNO2d\\_HRD/](https://avdc.gsfc.nasa.gov/pub/data/satellite/Aura/OMI/V03/L3/OMNO2d_HR/OMNO2d_HRD/) (last access: 3 December 2021).  
567 The CEDS emission inventory used in this work is also publicly available (<https://data.pnnl.gov/group/nodes/dataset/13488>) (last  
568 access: July 22, 2023). EPA AQS data of HCHO and NO<sub>2</sub> can be downloaded from: [https://www.epa.gov/outdoor-air-quality-](https://www.epa.gov/outdoor-air-quality-data/download-daily-data)  
569 [data/download-daily-data](https://www.epa.gov/outdoor-air-quality-data/download-daily-data) (last access: August 3, 2023).

570 *Supplement.* The supplement related to this article is available.

571 *Author Contributions.* MJ and SP obtained the funding for this project. MJ, SP, and RK were fundamental in developing the  
572 investigation strategy of this study. SJ, SP, SM, S M-H, and YS conducted the analysis which produce the results presented in this  
573 manuscript. Finally, MJ and SP were the primary authors which wrote the text of the manuscript.

574 *Competing interests.* The authors declare that they have no conflict of interest.

575 *Acknowledgements.* Computational resources were provided by the NASA High-End Computing Program through the NASA  
576 Advanced Supercomputing Division at NASA Ames Research Center. We acknowledge the United States Environmental

577 Protection Agency for the free availability of in situ data. The views, opinions and findings of this paper are those of the authors  
578 and should not be construed as an official NASA or United States Government position, policy, or decision.

579 *Financial support.* The MJ, SP, SM, RK, S M-H, and YS acknowledge funding support from the NASA Earth Science Division's  
580 Aura Science Team (NNH19ZDA001N-AURAST) as part of the Upper Atmosphere Research Program (UARP). A part of this  
581 material is based upon work supported by the NSF National Center for Atmospheric Research, which is a major facility sponsored  
582 by the U.S. National Science Foundation under Cooperative Agreement No. 1852977.

583



584 **References**

- 585 Accan, J. J. M., Pierce, R. B., Dickens, A. F., Adelman, Z., and Nergui, T.: Examining TROPOMI formaldehyde to nitrogen  
586 dioxide ratios in the Lake Michigan region: implications for ozone exceedances, *Atmos. Chem. Phys.*, 23, 7867–7885,  
587 <https://doi.org/10.5194/acp-23-7867-2023>, 2023.
- 588 Anderson, D. C., Nicely, J. M., Wolfe, G. M., Hanisco, T. F., Salawitch, R. J., Canty, T. P., Dickerson, R. R., Apel, E. C., Baidar,  
589 S., Bannan, T. J., Blake, N. J., Chen, D., Dix, B., Fernandez, R. P., Hall, S. R., Hornbrook, R. S., Gregory Huey, L., Josse, B.,  
590 Jöckel, P., Kinnison, D. E., Koenig, T. K., Le Breton, M., Marécal, V., Morgenstern, O., Oman, L. D., Pan, L. L., Percival,  
591 C., Plummer, D., Revell, L. E., Rozanov, E., Saiz-Lopez, A., Stenke, A., Sudo, K., Tilmes, S., Ullmann, K., Volkamer, R.,  
592 Weinheimer, A. J., and Zeng, G.: Formaldehyde in the Tropical Western Pacific: Chemical Sources and Sinks, Convective  
593 Transport, and Representation in CAM-Chem and the CCM1 Models, *J. Geophys. Res.-Atmos.*, 122, 11201–11226,  
594 <https://doi.org/10.1002/2016JD026121>, 2017.
- 595 Ayazpour, Z., Abad, G. G., Nowlan, C. R., Sun, K., Kwon, H. A., Miller, C. C., et al.: Aura Ozone Monitoring Instrument (OMI)  
596 Collection 4 Formaldehyde Product, ESS Open Archive, <http://dx.doi.org/10.22541/essoar.171804891.19520982/v1>, 2024.
- 597 Boersma, K. F., Eskes, H. J., Dirksen, R. J., van der A, R. J., Veefkind, J. P., Stammes, P., Huijnen, V., Kleipool, Q. L., Sneep,  
598 M., Claas, J., Leitão, J., Richter, A., Zhou, Y., and Brunner, D.: An improved tropospheric NO<sub>2</sub> column retrieval algorithm  
599 for the Ozone Monitoring Instrument, *Atmos. Meas. Tech.*, 4, 1905–1928, <https://doi.org/10.5194/amt-4-1905-2011>, 2011.
- 600 Boys, B., Martin, R., van Donkelaar, A., MacDonell, R., Hsu, C., Cooper, M., Yantosca, R., Lu, Z., Streets, D. G., Zhang, Q., and  
601 Wang, S.: Fifteen-year global time series of satellite-derived fine particulate matter, *Environ. Sci. Technol.*, 48, 11109–11118,  
602 2014.
- 603 Bucsela, E. J., Krotkov, N. A., Celarier, E. A., Lamsal, L. N., Swartz, W. H., Bhartia, P. K., Boersma, K. F., Veefkind, J. P.,  
604 Gleason, J. F., and Pickering, K. E.: A new stratospheric and tropospheric NO<sub>2</sub> retrieval algorithm for nadir-viewing satellite  
605 instruments: applications to OMI, *Atmos. Meas. Tech.*, 6, 2607–2626, <https://doi.org/10.5194/amt-6-2607-2013>, 2013.
- 606 Burrows, J. P., Weber, M., Buchwitz, M., Rozanov, V., Ladstätter-Weißenmayer, A., Richter, A., DeBeek, R., Hoogen, R.,  
607 Bramstedt, K., Eichmann, K.-U., Eisingera, M., and Pernerb, D.: The global ozone monitoring experiment (GOME): Mission  
608 concept and first scientific results, *J. Atmos. Sci.*, 56, 151–175, 1999.
- 609 Camalier, L., Cox, W., and Dolwick, P.: The effects of meteorology on ozone in urban areas and their use in assessing ozone  
610 trends, *Atmos. Environ.*, 41, 7127–7137, doi: 10.1016/j.atmosenv.2007.04.061, 2007.
- 611 Chance, K. V. and Spurr, R. J. D.: Ring effect studies: Rayleigh scattering, including molecular parameters for rotational Raman  
612 scattering, and the Fraunhofer spectrum, *Appl. Optics*, 36, 5224– 5230, doi:10.1364/AO.36.005224, 1997.
- 613 Chance, K.: Analysis of BrO measurements from the Global Ozone Monitoring Experiment, *Geophys. Res. Lett.*, 25, 3335–3338,  
614 <https://doi.org/10.1029/98GL52359>, 1998.
- 615 Chang, C. -Y., Faust, E., Hou, X., Lee, P., Kim, H. C., Hedquist, B. C., and Liao, K. -J.: Investigating ambient ozone formation  
616 regimes in neighboring cities of shale plays in the northeast United States using photochemical modeling and satellite  
617 retrievals, *Atmos. Environ.*, 142, 152–170. doi:10.1016/j.atmosenv.2016.06.058, 2016.
- 618 Choi, Y. and Souri, A.: Chemical condition and surface ozone in large cities of Texas during the last decade: observational evidence  
619 from OMI, CAMS, and Model Analysis, *Remote Sens. Environ.*, 168, 90–101, <https://doi.org/10.1016/j.rse.2015.06.026>,  
620 2015.

621 Choi, Y., Kim, H., Tong, D., and Lee, P.: Summertime weekly cycles of observed and modeled NO<sub>x</sub> and O<sub>3</sub> concentrations as a  
622 function of satellite-derived ozone production sensitivity and land use types over the Continental United States, *Atmos. Chem.*  
623 *Phys.*, 12, 6291–6307, doi:10.5194/acp-12-6291-2012, 2012.

624 Cooper, M. J., Martin, R. V., McLinden, C. A., and Brook, J. R.: Inferring ground-level nitrogen dioxide concentrations at fine  
625 spatial resolution applied to the TROPOMI satellite instrument, *Environ. Res. Lett.*, 15, 104013, [https://doi.org/10.1088/1748-](https://doi.org/10.1088/1748-9326/aba3a5)  
626 [9326/aba3a5](https://doi.org/10.1088/1748-9326/aba3a5), 2020.

627 Cooper, M. J., Martin, R. V., Hammer, M. S., Levelt, P. F., Veefkind, P., Lamsal, L. N., Krotkov, N. A., Brook, J. R., and  
628 McLinden, C. A.: Global fine-scale changes in ambient NO<sub>2</sub> during COVID-19 lockdowns, *Nature*, 601, 380–387,  
629 [10.1038/s41586-021-04229-0](https://doi.org/10.1038/s41586-021-04229-0), 2022.

630 Dave, J. V.: Meaning of successive iteration of the auxiliary equation in the theory of radiative transfer, *Astrophys. J.*, 140, 1292–  
631 1303, 1964.

632 De Smedt, I., Stavrakou, T., Hendrick, F., Danckaert, T., Vlemmix, T., Pinardi, G., Theys, N., Lerot, C., Gielen, C., Vigouroux,  
633 C., Hermans, C., Fayt, C., Veefkind, P., Müller, J.-F., and Van Roozendael, M.: Diurnal, seasonal and long-term variations of  
634 global formaldehyde columns inferred from combined OMI and GOME-2 observations, *Atmos. Chem. Phys.*, 15, 12519–  
635 12545, <https://doi.org/10.5194/acp-15-12519-2015>, 2015.

636 De Smedt, I., Theys, N., Yu, H., Danckaert, T., Lerot, C., Compernelle, S., Van Roozendael, M., Richter, A., Hilboll, A., Peters,  
637 E., Pedernana, M., Loyola, D., Beirle, S., Wagner, T., Eskes, H., van Geffen, J., Boersma, K. F., and Veefkind, P.: Algorithm  
638 theoretical baseline for formaldehyde retrievals from S5P TROPOMI and from the QA4ECV project, *Atmos. Meas. Tech.*,  
639 11, 2395–2426, <https://doi.org/10.5194/amt-11-2395-2018>, 2018.

640 Demuzere, M., He, C., Martilli, A., Zonato, A.: Technical documentation for the hybrid 100-m global land cover dataset with Local  
641 Climate Zones for WRF. <https://doi.org/10.5281/zenodo.7670791>, 2023.

642 Dobber, M., Kleipool, Q., Dirksen, R., Levelt, P., Jaross, G., Taylor, S., Kelly, T., and Flynn, L.: Validation of ozone monitoring  
643 instrument level-1b data products, *J. Geophys. Res.*, 113, D15S06, <https://doi.org/10.1029/2007JD008665>, 2008.

644 Duncan, B., Yoshida, Y., Olson, J., Sillman, S., Martin, R., Lamsal, L., Hu, Y., Pickering, K., Retscher, D., Allen, D., and Crawford,  
645 J.: Application of OMI observations to a space-based indicator of NO<sub>x</sub> and VOC controls on surface ozone formation, *Atmos.*  
646 *Environ.*, 44, 2213–2223, <https://doi.org/10.1016/j.atmosenv.2010.03.010>, 2010.

647 Fan, C., Li, Z., Li, Y., Dong, J., van der A, R., and de Leeuw, G.: Variability of NO<sub>2</sub> concentrations over China and effect on air  
648 quality derived from satellite and ground-based observations, *Atmos. Chem. Phys.*, 21, 7723–7748,  
649 <https://doi.org/10.5194/acp-21-7723-2021>, 2021.

650 GBD 2019 Risk Factor Collaborators: Global burden of 87 risk factors in 204 countries and territories, 1990–2019: a systematic  
651 analysis for the Global Burden of Disease Study 2019, *The Lancet*, 396, 1223–1249, [https://doi.org/10.1016/s0140-](https://doi.org/10.1016/s0140-6736(20)30752-2)  
652 [6736\(20\)30752-2](https://doi.org/10.1016/s0140-6736(20)30752-2), 2020.

653 Geddes, J. A., Martin, R. V., Boys, B. L., and van Donkelaar, A.: Long term trends worldwide in ambient NO<sub>2</sub> concentrations  
654 inferred from satellite observations, *Environ. Health Perspect.*, doi:10.1289/ehp.1409567, 2016.

655 Goldberg, D. L., Anenberg, S. C., Griffin, D., McLinden, C. A., Lu, Z., and Streets, D. G.: Disentangling the Impact of the COVID-  
656 19 Lockdowns on Urban NO<sub>2</sub> From Natural Variability, *Geophys. Res. Lett.*, 47, e2020GL089269,  
657 <https://doi.org/10.1029/2020GL089269>, 2020.

658 González Abad, G., Liu, X., Chance, K., Wang, H., Kurosu, T. P., and Suleiman, R.: Updated Smithsonian Astrophysical  
659 Observatory Ozone Monitoring Instrument (SAO OMI) formaldehyde retrieval, *Atmos. Meas. Tech.*, 8, 19–32,  
660 doi:10.5194/amt-8-19-2015, 2015.

661 González Abad, G., Souri, A. H., Bak, J., Chance, K., Flynn, L. E., Krotkov, N. A., Lamsal, L., Li, C., Liu, X., Miller, C. C.,  
662 Nowlan, C. R., Suleiman, R., and Wang, H.: Five decades observing Earth's atmospheric trace gases using ultraviolet and  
663 visible backscatter solar radiation from space, *J. Quant. Spectrosc. Ra.*, 238, 106478,  
664 <https://doi.org/10.1016/j.jqsrt.2019.04.030>, 2019.

665 Guenther, A., Hewitt, N., Erickson, D., Fall, R., Geron, C., Graedel, T., Harley, P., Klinger, L., Lerdau, M., McKay, W., Pierce,  
666 T., Scholes, B., Steinbrecher, R., Tallamraju, R., Taylor, J., and Zimmerman, P.: A global model of natural volatile organic  
667 compound emissions, *J. Geophys. Res.*, 100, 8873–8892, 1995.

668 He, G., Pan, Y. and Tanaka, T.: The short-term impacts of COVID-19 lockdown on urban air pollution in China, *Nature*  
669 *Sustainability*, 3(12), 1005–1011, <https://doi.org/10.1038/s41893-020-0581-y>, 2020.

670 Hilboll, A., Richter, A., and Burrows, J. P.: Long-term changes of tropospheric NO<sub>2</sub> over megacities derived from multiple satellite  
671 instruments, *Atmos. Chem. Phys.*, 13, 4145–4169, <https://doi.org/10.5194/acp-13-4145-2013>, 2013.

672 Itahashi, S., Irie, H., Shimadera, H., and Chatani, S.: Fifteen-Year Trends (2005–2019) in the Satellite-Derived Ozone-Sensitive  
673 Regime in East Asia: A Gradual Shift from VOC-Sensitive to NO<sub>x</sub>-Sensitive, *Remote Sens.*, 14, 4512,  
674 <https://doi.org/10.3390/rs14184512>, 2022.

675 Jacob, D. J., Horowitz, L. W., Munger, J. W., Heikes, B. G., Dickerson, R. R., Artz, R. S., and Keene, W. C.: Seasonal transition  
676 from NO<sub>x</sub>- to hydrocarbon-limited conditions for ozone production over the eastern United States in September, *J. Geophys.*  
677 *Res.-Atmo.*, 100, 9315–9324, <https://doi.org/10.1029/94JD03125>, 1995.

678 Jin, X., and Holloway, T.: Spatial and temporal variability of ozone sensitivity over China observed from the Ozone Monitoring  
679 Instrument, *J. Geophys. Res. Atmos.*, 120, 7229–7246, doi:10.1002/2015JD023250, 2015.

680 Jin, X., Fiore, A. M., Murray, L. T., Valin, L. C., Lamsal, L. N., Duncan, B., Boersma, K. F., De Smedt, I., Abad, G. G., Chance,  
681 K., and Tonnesen, G. S.: Evaluating a Space-Based Indicator of Surface Ozone-NO<sub>x</sub>-VOC Sensitivity Over Midlatitude  
682 Source Regions and Application to Decadal Trends, *J. Geophys. Res.-Atmos.*, 122, 10439–10461,  
683 <https://doi.org/10.1002/2017JD026720>, 2017.

684 Jin, X., Fiore, A. M., and Geigert, M.: Using satellite observed formaldehyde (HCHO) and nitrogen dioxide (NO<sub>2</sub>) as an indicator  
685 of ozone sensitivity in a SIP, HAQAST Tech. Guid. Doc. No. 1, doi:10.7916/D8M34C7V, 2018.

686 Jin, X., Fiore, A., Boersma, K. F., De Smedt, I., and Valin, L.: Inferring Changes in Summertime Surface Ozone–NO<sub>x</sub>–VOC  
687 Chemistry over U.S. Urban Areas from Two Decades of Satellite and Ground-Based Observations, *Environ. Sci. Technol.*,  
688 54, 6518–6529, <https://doi.org/10.1021/acs.est.9b07785>, 2020.

689 Johnson, M. S., Souri, A. H., Philip, S., Kumar, R., Naeger, A., Geddes, J., Judd, L., Janz, S., Chong, H., and Sullivan, J.: Satellite  
690 remote-sensing capability to assess tropospheric-column ratios of formaldehyde and nitrogen dioxide: case study during the  
691 Long Island Sound Tropospheric Ozone Study 2018 (LISTOS 2018) field campaign, *Atmos. Meas. Tech.*, 16, 2431–2454,  
692 <https://doi.org/10.5194/amt-16-2431-2023>, 2023.

693 Kharol, S. K., Martin, R. V., Philip, S., Boys, B., Lamsal, L. N., Jerrett, M., Brauer, M., Crouse, D. L., McLinden, C., and Burnett,  
694 R. T.: Assessment of the magnitude and recent trends in satellite-derived ground-level nitrogen dioxide over North America,  
695 *Atmos. Environ.*, 118, 236–245, <https://doi.org/10.1016/j.atmosenv.2015.08.011>, 2015.

696 Kleinman, L. I.: Low and high NO<sub>x</sub> tropospheric photochemistry, *J. Geophys. Res.*, 99, 16831–16838, 1994.

697 Kleinman, L. I., Daum, P. H., Lee, Y. N., Nunnermacker, L. J., Springston, S. R., Weinstein-Lloyd, J., and Rudolph, J.: A  
698 comparative study of ozone production in five US metropolitan areas, *J. Geophys. Res.-Atmos.*, 110, D02301,  
699 doi:10.1029/2004JD005096, 2005.

700 Kleipool, Q., Rozemeijer, N., van Hoek, M., Leloux, J., Loots, E., Ludewig, A., van der Plas, E., Adrichem, D., Harel, R., Spronk,  
701 S., ter Linden, M., Jaross, G., Haffner, D., Veefkind, P., and Levelt, P. F.: Ozone Monitoring Instrument (OMI) collection 4:  
702 establishing a 17-year-long series of detrended level-1b data, *Atmos. Meas. Tech.*, 15, 3527–3553,  
703 <https://doi.org/10.5194/amt-15-3527-2022>, 2022.

704 Koplitz, S., Simon, H., Henderson, B., Liljegren, J., Tonnesen, G., Whitehill, A., and Wells, B.: Changes in Ozone Chemical  
705 Sensitivity in the United States from 2007 to 2016, *ACS Environ. Au*, 2, 206–222,  
706 <https://doi.org/10.1021/ACSENVIRONAU.1C00029>, 2021.

707 Krotkov, N. A., McLinden, C. A., Li, C., Lamsal, L. N., Celarier, E. A., Marchenko, S. V., Swartz, W. H., Bucsela, E. J., Joiner,  
708 J., Duncan, B. N., Boersma, K. F., Veefkind, J. P., Levelt, P. F., Fioletov, V. E., Dickerson, R. R., He, H., Lu, Z., and Streets,  
709 D. G.: Aura OMI observations of regional SO<sub>2</sub> and NO<sub>2</sub> pollution changes from 2005 to 2015, *Atmos. Chem. Phys.*, 16,  
710 4605–4629, <https://doi.org/10.5194/acp-16-4605-2016>, 2016.

711 Krotkov, N. A., Lamsal, L. N., Celarier, E. A., Swartz, W. H., Marchenko, S. V., Bucsela, E. J., Chan, K. L., Wenig, M., and Zara,  
712 M.: The version 3 OMI NO<sub>2</sub> standard product, *Atmos. Meas. Tech.*, 10, 3133–3149, [https://doi.org/10.5194/amt-10-3133-](https://doi.org/10.5194/amt-10-3133-2017)  
713 2017, 2017.

714 Lamsal, L. N., Martin, R. V., Steinbacher, M., Celarier, E. A., Bucsela, E., Dunlea, E. J., and Pinto, J.: Ground level nitrogen  
715 dioxide concentrations inferred from the satellite-borne Ozone Monitoring Instrument, *J. Geophys. Res.*, 113, D16308,  
716 <https://doi.org/10.1029/2007JD009235>, 2008.

717 Lamsal, L. N., Martin, R. V., van Donkelaar, A., Celarier, E. A., Bucsela, E. J., Boersma, K. F., Dirksen, R., Luo, C., and Wang,  
718 Y.: Indirect validation of tropospheric nitrogen dioxide retrieved from the OMI satellite instrument: Insight into the seasonal  
719 variation of nitrogen oxides at northern midlatitudes, *J. Geophys. Res.*, 115, D05302, <https://doi.org/10.1029/2009JD013351>,  
720 2010.

721 Lamsal, L. N., Duncan, B. N., Yoshida, Y., Krotkov, N. A., Pickering, K. E., Streets, D. G., and Lu, Z.: U.S. NO<sub>2</sub> trends (2005–  
722 2013): EPA Air Quality System (AQS) data versus improved observations from the Ozone Monitoring Instrument (OMI),  
723 *Atmos. Environ.*, 110, 130–143, doi:10.1016/j.atmosenv.2015.03.055, 2015.

724 Levelt, P. F., Hilsenrath, E., Leppelmeier, G. W., Oord, G. H. J. Van Den, Bhartia, P. K., Tamminen, J., De Haan, J. F., and  
725 Veefkind, J. P.: Science Objectives of the Ozone Monitoring Instrument, *IEEE T. Geosci. Remote Sens.*, 44, 1199–1208,  
726 2006.

727 Levelt, P. F., Joiner, J., Tamminen, J., Veefkind, J. P., Bhartia, P. K., Stein Zweers, D. C., Duncan, B. N., Streets, D. G., Eskes,  
728 H., van der A, R., McLinden, C., Fioletov, V., Carn, S., de Laat, J., DeLand, M., Marchenko, S., McPeters, R., Ziemke, J., Fu,  
729 D., Liu, X., Pickering, K., Apituley, A., González Abad, G., Arola, A., Boersma, F., Chan Miller, C., Chance, K., de Graaf,  
730 M., Hakkarainen, J., Hassinen, S., Ialongo, I., Kleipool, Q., Krotkov, N., Li, C., Lamsal, L., Newman, P., Nowlan, C.,  
731 Suleiman, R., Tilstra, L. G., Torres, O., Wang, H., and Wargan, K.: The Ozone Monitoring Instrument: overview of 14 years  
732 in space, *Atmos. Chem. Phys.*, 18, 5699–5745, <https://doi.org/10.5194/acp-18-5699-2018>, 2018.

733 Li, Y., Lau, A. K. H., Fung, J. C. H., Zheng, J. Y., Zhong, L. J., and Louie, P. K. K.: Ozone source apportionment (OSAT) to  
734 differentiate local regional and super-regional source contributions in the Pearl River Delta region, China, *J. Geophys. Res.-*  
735 *Atmos.*, 117, 1–18, <https://doi.org/10.1029/2011JD017340>, 2012.

736 Mahajan, A. S., De Smedt, I., Biswas, M. S., Ghude, S., Fadnavis, S., Roy, C., and van Roozendaal, M.: Inter-annual variations in  
737 satellite observations of nitrogen dioxide and formaldehyde over India, *Atmos. Environ.*, 116, 194–201,  
738 <https://doi.org/10.1016/j.atmosenv.2015.06.004>, 2015.

739 Marais, E. A., Jacob, D. J., Kurosu, T. P., Chance, K., Murphy, J. G., Reeves, C., Mills, G., Casadio, S., Millet, D. B., Barkley, M.  
740 P., Paulot, F., and Mao, J.: Isoprene emissions in Africa inferred from OMI observations of formaldehyde columns, *Atmos.*  
741 *Chem. Phys.*, 12, 6219–6235, <https://doi.org/10.5194/acp-12-6219-2012>, 2012.

742 Marchenko, S., Krotkov, N., Lamsal, L., Celarier, E., Swartz, W., and Bucsele, E.: Revising the slant column density retrieval of  
743 nitrogen dioxide observed by the Ozone Monitoring Instrument, *J. Geophys. Res.*, 120, 5670–5692,  
744 <https://doi.org/10.1002/2014JD022913>, 2015.

745 Martin, R. V., Fiore, A. M., and Van Donkelaar, A.: Space-based diagnosis of surface ozone sensitivity to anthropogenic  
746 emissions, *Geophys. Res. Lett.*, 31, L06120. doi:10.1029/2004GL019416, 2004.

747 McDuffie, E. E., Smith, S. J., O'Rourke, P., Tibrewal, K., Venkataraman, C., Marais, E. A., Zheng, B., Crippa, M., Brauer, M.,  
748 and Martin, R. V.: A global anthropogenic emission inventory of atmospheric pollutants from sector- and fuel-specific sources  
749 (1970–2017): an application of the Community Emissions Data System (CEDS), *Earth Syst. Sci. Data*, 12, 3413–3442,  
750 <https://doi.org/10.5194/essd-12-3413-2020>, 2020.

751 Milford, J. B., Gao, D. F., Sillman, S., Blossey, P., and Russell, A. G.: Total reactive nitrogen (NO<sub>y</sub>) as an indicator of the  
752 sensitivity of ozone to reductions in hydrocarbon and NO<sub>x</sub> emissions, *J. Geophys. Res.-Atmos.*, 99, 3533–3542,  
753 <https://doi.org/10.1029/93jd03224>, 1994.

754 Millet, D. B., Jacob, D. J., Boersma, K. F., Fu, T.-M., Kurosu, T. P., Chance, K., Heald, C. L., and Guenther, A.: Spatial distribution  
755 of isoprene emissions from North America derived from formaldehyde column measurements by the OMI satellite sensor, *J.*  
756 *Geophys. Res.*, 113, D02307, <https://doi.org/10.1029/2007JD008950>, 2008.

757 Monks, P. S., Archibald, A. T., Colette, A., Cooper, O., Coyle, M., Derwent, R., Fowler, D., Granier, C., Law, K. S., Mills, G. E.,  
758 Stevenson, D. S., Tarasova, O., Thouret, V., von Schneidmesser, E., Sommariva, R., Wild, O., and Williams, M. L.:  
759 Tropospheric ozone and its precursors from the urban to the global scale from air quality to short-lived climate forcer, *Atmos.*  
760 *Chem. Phys.*, 15, 8889–8973, <https://doi.org/10.5194/acp-15-8889-2015>, 2015.

761 Nussbaumer, C. M., Pozzer, A., Tadic, I., Röder, L., Obersteiner, F., Harder, H., Lelieveld, J., and Fischer, H.: Tropospheric ozone  
762 production and chemical regime analysis during the COVID-19 lockdown over Europe, *Atmos. Chem. Phys.*, 22, 6151–6165,  
763 <https://doi.org/10.5194/acp-22-6151-2022>, 2022.

764 Palmer, P. I., Jacob, D. J., Chance, K., Martin, R. V., Spurr, R. J. D., Kurosu, T. P., Bey, I., Yantosca, R., Fiore, A., and Li, Q.:  
765 Air mass factor formulation for spectroscopic measurements from satellites: Application to formaldehyde retrievals from the  
766 Global Ozone Monitoring Experiment, *J. Geophys. Res.-Atmos.*, 106, 14539–14550, <https://doi.org/10.1029/2000JD900772>,  
767 2001.

768 Pei, C. L., Yang, W. Q., Zhang, Y. L., Song, W., Xiao, S. X., Wang, J., Zhang, J. P., Zhang, T., Chen, D. H., Wang, Y. J., Chen,  
769 Y. N., and Wang, X. M.: Decrease in ambient volatile organic compounds during the COVID-19 lockdown period in the Pearl  
770 River Delta region, South China, *Sci. Total Environ.*, 823, 153720, <https://doi.org/10.1016/j.scitotenv.2022.153720>, 2022.

771 Philip, S., Martin, R. V., van Donkelaar, A., Lo, J. W., Wang, Y., Chen, D., Zhang, L., Kasibhatla, P. S., Wang, S. W., Zhang, Q.,  
772 Lu, Z., Streets, D. G., Bittman, S., and Macdonald, D. J.: Global chemical composition of ambient fine particulate matter for  
773 exposure assessment, *Environ. Sci. Technol.*, 48, 13060-13068, doi:10.1021/es502965b, 2014.

774 Schenkeveld, V. M. E., Jaross, G., Marchenko, S., Haffner, D., Kleipool, Q. L., Rozemeijer, N. C., Veeffkind, J. P., and Levelt, P.  
775 F.: In-flight performance of the Ozone Monitoring Instrument, *Atmos. Meas. Tech.*, 10, 1957–1986,  
776 <https://doi.org/10.5194/amt-10-1957-2017>, 2017.

777 Schoeberl, M. R., Douglass, A. R., Hilsenrath, E., Bhartia, P. K., Beer, R., Waters, J. W., Gunson, M. R., Froidevaux, L., Gille, J.  
778 C., Barnett, J. J., Levelt, P. F., and DeCola, P.: Overview of the EOS aura mission, *IEEE T. Geosci. Remote Sens.*, 44, 1066–  
779 1072, doi:10.1109/TGRS.2005.861950, 2006.

780 Schroeder, J. R., Crawford, J. H., Fried, A., Walega, J., Weinheimer, A., Wisthaler, A., Müller, M., Mikoviny, T., Chen, G., Shook,  
781 M., Blake, D. R., and Tonnesen, G. S.: New insights into the column CH<sub>2</sub>ONO<sub>2</sub> ratio as an indicator of near-surface ozone  
782 sensitivity, *J. Geophys. Res.-Atmos.*, 122, 8885–8907, <https://doi.org/10.1002/2017JD026781>, 2017.

783 Seinfeld, J. H. and Pandis, S. N.: *Atmospheric Chemistry and Physics: From Air Pollution to Climate Change*, John Wiley and  
784 Sons, Hoboken, ISBN: 978-1-118-94740-1, 2016.

785 Shen, L., Jacob, D. J., Liu, X., Huang, G., Li, K., Liao, H., and Wang, T.: An evaluation of the ability of the Ozone Monitoring  
786 Instrument (OMI) to observe boundary layer ozone pollution across China: application to 2005–2017 ozone trends, *Atmos.*  
787 *Chem. Phys.*, 19, 6551–6560, <https://doi.org/10.5194/acp-19-6551-2019>, 2019.

788 Sillman, S.: The use of NO<sub>y</sub>, H<sub>2</sub>O<sub>2</sub>, and HNO<sub>3</sub> as indicators for O<sub>3</sub>-NO<sub>x</sub>-hydrocarbon sensitivity in urban locations, *J. Geophys.*  
789 *Res. Atmos.*, 100, 14175-14188, doi:10.1029/94JD02953, 1995.

790 Sillman, S.: The relation between ozone, NO<sub>x</sub>, and hydrocarbons in urban and polluted rural environments, *Atmos. Environ.*, 33,  
791 1821–1845, 1999.

792 Sillman, S., Logan, J. A., and Wofsy, S. C.: The sensitivity of ozone to nitrogen oxides and hydrocarbons in regional ozone  
793 episodes, *J. Geophys. Res.*, 95, 1837-1851, doi: 10.1029/JD095iD02p01837, 1990.

794 Souri, A. H., Choi, Y., Jeon, W., Woo, J. -H., Zhang, Q., and Kurokawa J.-i.: Remote sensing evidence of decadal changes in  
795 major tropospheric ozone precursors over East Asia, *J. Geophys. Res. Atmos.*, 122, 2474-2492, doi:10.1002/2016JD025663,  
796 2017.

797 Souri, A. H., Nowlan, C. R., Wolfe, G. M., Lamsal, L. N., Chan Miller, C. E., Abad, G. G., Janz, S. J., Fried, A., Blake, D. R.,  
798 Weinheimer, A. J., Diskin, G. S., Liu, X., and Chance, K.: Revisiting the effectiveness of HCHO/NO<sub>2</sub> ratios for inferring  
799 ozone sensitivity to its precursors using high resolution airborne remote sensing observations in a high ozone episode during  
800 the KORUS-AQ campaign, *Atmos. Environ.*, 224, 117341, <https://doi.org/10.1016/j.atmosenv.2020.117341>, 2020.

801 Souri, A. H., Chance, K., Sun, K., Liu, X., and Johnson, M. S.: Dealing with spatial heterogeneity in pointwise-to-gridded- data  
802 comparisons, *Atmos. Meas. Tech.*, 15, 41–59, <https://doi.org/10.5194/amt-15-41-2022>, 2022.

803 Souri, A. H., Johnson, M. S., Wolfe, G. M., Crawford, J. H., Fried, A., Wisthaler, A., Brune, W. H., Blake, D. R., Weinheimer, A.  
804 J., Verhoelst, T., Compennolle, S., Pinardi, G., Vigouroux, C., Langerock, B., Choi, S., Lamsal, L., Zhu, L., Sun, S., Cohen,  
805 R. C., Min, K.-E., Cho, C., Philip, S., Liu, X., and Chance, K.: Characterization of errors in satellite-based HCHO/NO<sub>2</sub>  
806 tropospheric column ratios with respect to chemistry, column-to-PBL translation, spatial representation, and retrieval  
807 uncertainties, *Atmos. Chem. Phys.*, 23, 1963–1986, <https://doi.org/10.5194/acp-23-1963-2023>, 2023a.

808 Souri, A. H., Kumar, R., Chong H., Golbazi, M., Knowland, K. E., Geddes, J., and Johnson, M. S.: Decoupling in the vertical  
809 shape of HCHO during a sea breeze event: The effect on trace gas satellite retrievals and column-to-surface translation,  
810 *Atmospheric Environment*, 309, <https://doi.org/10.1016/j.atmosenv.2023.119929>, 2023b.

811 Spurr, R. J. D.: VLIDORT: a linearized pseudo-spherical vector discrete ordinate radiative transfer code for forward model and  
812 retrieval studies in multilayer multiple scattering media, *J. Quant. Spectrosc. Rad. Trans.*, 102, 316–421,  
813 <https://doi.org/10.1016/j.jqsrt.2006.05.005>, 2006.

814 Stewart, I. D. and Oke, T. R.: Local Climate Zones for Urban Temperature Studies, *B. Am. Meteorol. Soc.*, 93, 1879–1900,  
815 <https://doi.org/10.1175/BAMS-D-11-00019.1>, 2012.

816 Tai, A., Martin, M., and Heald, C.: Threat to future global food security from climate change and ozone air pollution, *Nature Clim*  
817 *Change*, 4, 817–821, <https://doi.org/10.1038/nclimate2317>, 2014.

818 Tao, M., Fiore, A. M., Jin, X., Schiferl, L. D., Commane, R., Judd, L. M., Janz, S., Sullivan, J. T., Miller, P. J., Karambelas, A.,  
819 Davis, S., Tzortziou, M., Valin, L., Whitehill, A., Civerolo, K., and Tian, Y.: Investigating changes in ozone formation  
820 chemistry during summertime pollution vents over the northeastern United States, *Environ. Sci. Technol.*, 56, 15312–15327,  
821 <https://doi.org/10.1021/acs.est.2c02972>, 2022.

822 Tonnesen, G. S., and Dennis, R. L.: Analysis of radical propagation efficiency to assess O<sub>3</sub> sensitivity to hydrocarbons and NO<sub>x</sub>:  
823 2. Long-lived species as indicators of O<sub>3</sub> concentration sensitivity, *J. Geophys. Res. Atmos.*, 105, 9227–9241.  
824 Doi:10.1029/1999JD900372, 2000.

825 US Environmental Protection Agency (US EPA): Air Quality Criteria for Ozone and Related Photochemical Oxidants (2006 Final),  
826 U.S. Environmental Protection Agency, Washington, DC, EPA/600/R-05/004aF-cF, 2006.

827 Wang, W., van der A, R., Ding, J., van Weele, M., and Cheng, T.: Spatial and temporal changes of the ozone sensitivity in China  
828 based on satellite and ground-based observations, *Atmos. Chem. Phys.*, 21, 7253–7269, [https://doi.org/10.5194/acp-21-7253-](https://doi.org/10.5194/acp-21-7253-2021)  
829 [2021](https://doi.org/10.5194/acp-21-7253-2021), 2021.

830 Witte, J., Duncan, B., Douglass, A., Kurosu, T., Chance, K., and Retscher, C.: The unique OMI HCHO NO<sub>2</sub> feature during the  
831 2008 Beijing Olympics: Implications for ozone production sensitivity, *Journal: Atmospheric Environment*, 45, 3103–3111,  
832 <https://doi.org/10.1016/j.atmosenv.2011.03.015>, 2011.

833 Wu, S., Duncan, B. N., Jacob, D. J., Fiore, A. M. and Wild, O.: Chemical nonlinearities in relating intercontinental ozone pollution  
834 to anthropogenic emissions, *Geophys. Res. Lett.*, 36, L05806, doi:10.1029/2008GL036607, 2009.

835 Zhang, L., Jacob, D. J., Kopacz, M., Henze, D. K., Singh, K., and Jaffe, D. A.: Intercontinental source attribution of ozone pollution  
836 at western U.S. sites using an adjoint method, *Geophys. Res. Lett.*, 36, L11810, <https://doi.org/10.1029/2009GL037950>, 2009.

837 Zhu, L., Jacob, D. J., Mickley, L. J., Marais, E. A., Cohan, D. S., Yoshida, Y., Duncan, B. N., González Abad, G., and Chance, K.  
838 V.: Anthropogenic emissions of highly reactive volatile organic compounds in eastern Texas inferred from oversampling of  
839 satellite (OMI) measurements of HCHO columns, *Environ. Res. Lett.*, 9, 114004, [https://doi.org/10.1088/1748-](https://doi.org/10.1088/1748-9326/9/11/114004)  
840 [9326/9/11/114004](https://doi.org/10.1088/1748-9326/9/11/114004), 2014.

841 Zhu, L., Jacob, D. J., Kim, P. S., Fisher, J. A., Yu, K., Travis, K. R., Mickley, L. J., Yantosca, R. M., Sulprizio, M. P., De Smedt,  
842 I., González Abad, G., Chance, K., Li, C., Ferrare, R., Fried, A., Hair, J. W., Hanisco, T. F., Richter, D., Jo Scarino, A.,  
843 Walega, J., Weibring, P., and Wolfe, G. M.: Observing atmospheric formaldehyde (HCHO) from space: validation and  
844 intercomparison of six retrievals from four satellites (OMI, GOME2A, GOME2B, OMPS) with SEAC4RS aircraft

845 observations over the southeast US, *Atmos. Chem. Phys.*, 16, 13477–13490, <https://doi.org/10.5194/acp-16-13477-2016>,  
846 2016.

847 Zhu, L., Jacob, D. J., Keutsch, F. N., Mickley, L. J., Scheffe, R., Strum, M., González Abad, G., Chance, K., Yang, K.,  
848 Rappenglück, B., Millet, D. B., and Baasandorj, M.: Formaldehyde (HCHO) as a Hazardous Air Pollutant: Mapping surface  
849 air concentrations from satellite and inferring cancer risks in the United States, *Environ. Sci. Technol.*, 51, 5650–5657,  
850 <https://doi.org/10.1021/acs.est.7b01356>, 2017a.

851 Zhu, L., Mickley, L. J., Jacob, D. J., Marais, E. A., Sheng, J., Hu, L., González Abad, G., and Chance, K.: Long-term (2005–2014)  
852 trends in formaldehyde (HCHO) columns across North America as seen by the OMI satellite instrument: Evidence of changing  
853 emissions of volatile organic compounds, *Geophys. Res. Lett.*, 44, 7079–7086, <https://doi.org/10.1002/2017GL073859>,  
854 2017b.

855 Zhu, L., González Abad, G., Nowlan, C. R., Chan Miller, C., Chance, K., Apel, E. C., DiGangi, J. P., Fried, A., Hanisco, T. F.,  
856 Hornbrook, R. S., Hu, L., Kaiser, J., Keutsch, F. N., Permar, W., St. Clair, J. M., and Wolfe, G. M.: Validation of satellite  
857 formaldehyde (HCHO) retrievals using observations from 12 aircraft campaigns, *Atmos. Chem. Phys.*, 20, 12329–12345,  
858 <https://doi.org/10.5194/acp-20-12329-2020>, 2020.

859



860 **Tables**

861

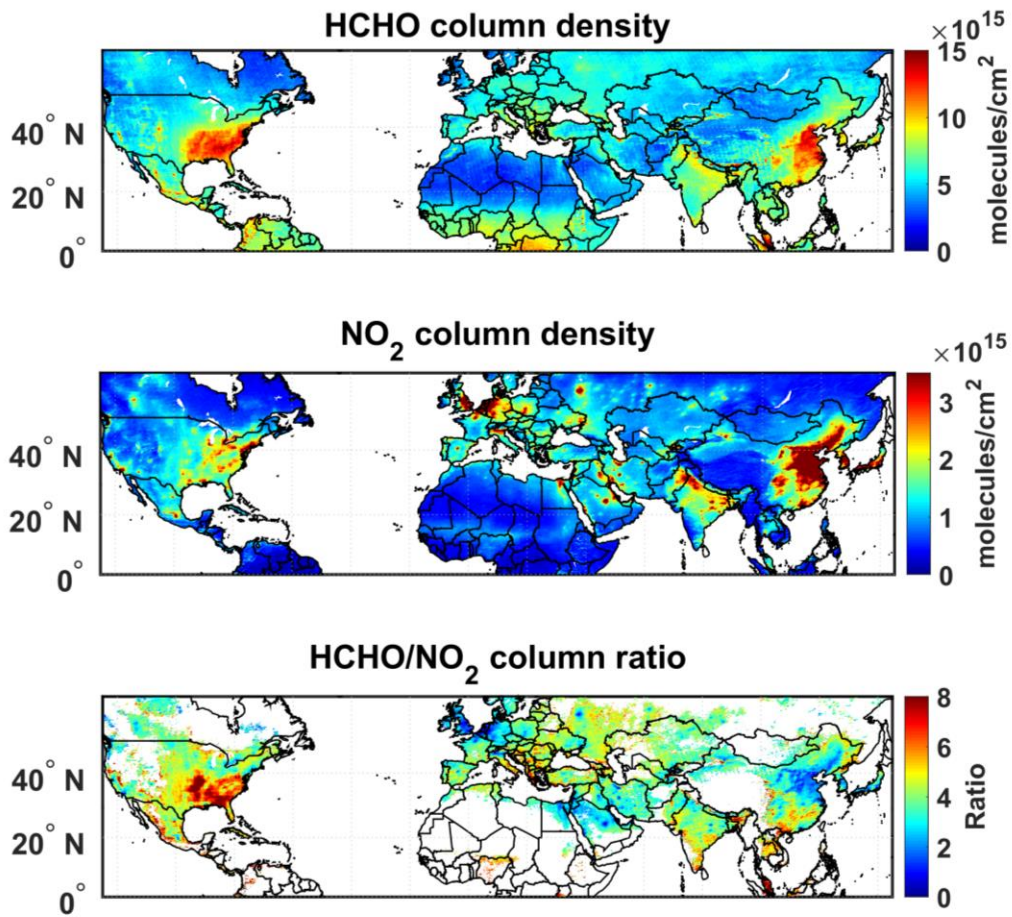
862 **Table 1. Statistics of the correlation of OMI and AQS (“Obs.”) normalized trends for HCHO, NO<sub>2</sub>, and FNRs**  
 863 **for major cities in the US and the average of all cities in the US (USA urban areas) between 2005-2019. Slopes**  
 864 **of the trends for each species (units of yr<sup>-1</sup>) are also provided. The values in italic font are linear regression**  
 865 **slopes which are statistically significant at a 95% confidence level (p<0.05).**

Cities	Corr. HCHO	Slope HCHO Obs.	Slope HCHO OMI	Corr. NO <sub>2</sub>	Slope NO <sub>2</sub> Obs.	Slope NO <sub>2</sub> OMI	Corr. FNR	Slope FNR Obs.	Slope FNR OMI
New York	0.01	<i>0.10</i>	0.05	0.91	<i>-0.21</i>	<i>-0.20</i>	0.78	<i>0.20</i>	<i>0.20</i>
Los Angeles	-0.01	-0.14	0.14	0.98	<i>-0.21</i>	<i>-0.22</i>	0.84	<i>0.17</i>	<i>0.22</i>
Chicago	NaN	NaN	0.07	0.91	<i>-0.22</i>	<i>-0.21</i>	NaN	NaN	<i>0.18</i>
Washington DC	0.38	<i>0.11</i>	0.05	0.89	<i>-0.19</i>	<i>-0.20</i>	0.77	<i>0.18</i>	<i>0.21</i>
Pittsburgh	0.51	0.06	0.10	0.64	<i>-0.21</i>	<i>-0.16</i>	0.55	<i>0.22</i>	<i>0.16</i>
Atlanta	NaN	NaN	-0.07	0.33	-0.01	<i>-0.17</i>	NaN	NaN	<i>0.18</i>
Houston	0.40	<i>-0.18</i>	-0.06	0.79	<i>-0.17</i>	<i>-0.17</i>	-0.27	<i>-0.12</i>	<i>0.13</i>
USA urban areas	0.24	-0.05	<i>0.15</i>	0.98	<i>-0.21</i>	<i>-0.20</i>	0.91	<i>0.21</i>	<i>0.21</i>

866 Correlation values are the correlation coefficient (R).

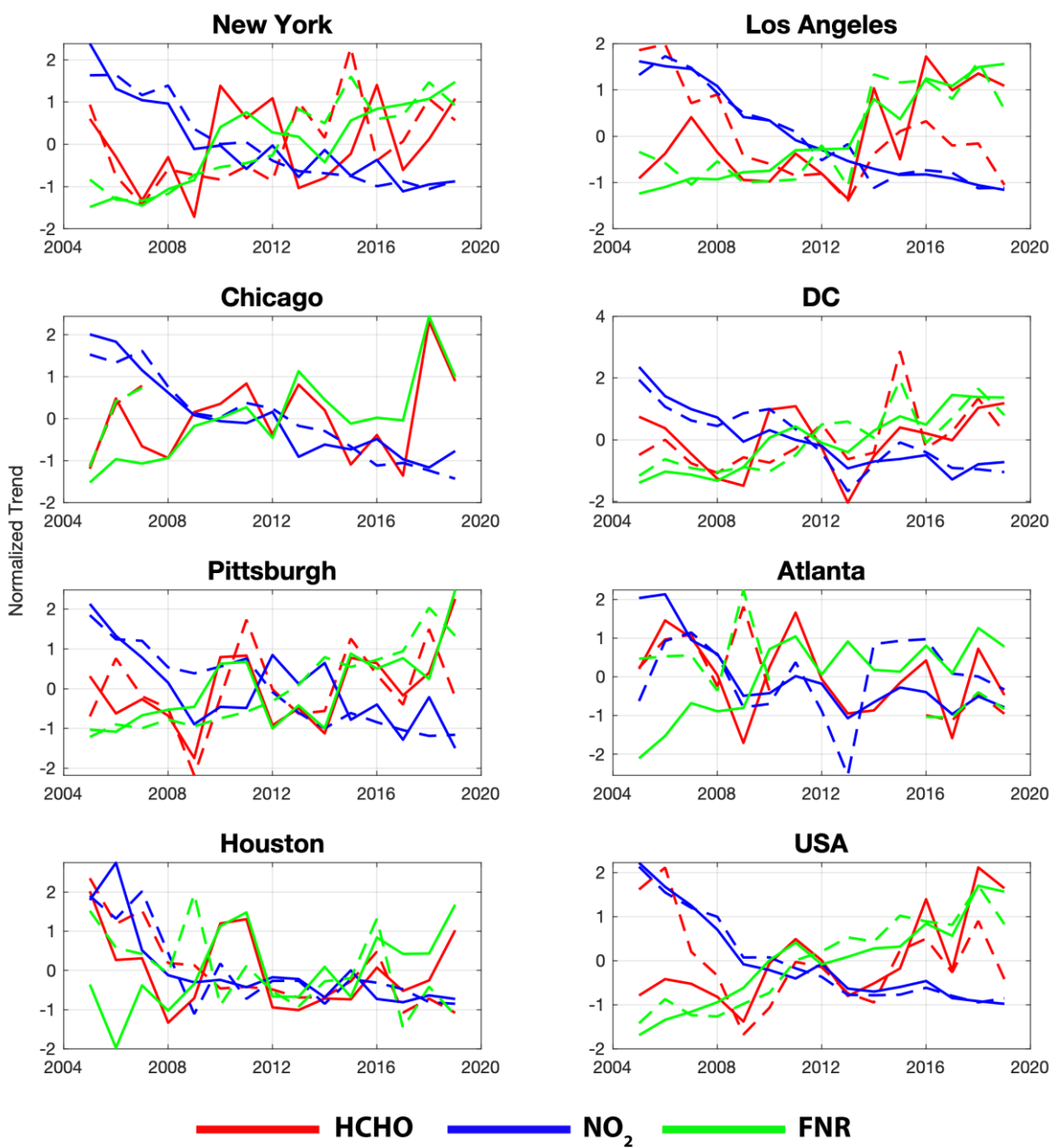
867 NaN values indicate cities where particular species data is not available for all years between 2005-2019.

868



870  
 871 **Figure 1: OMI-derived multi-year (2005-2021) summer mean (June-August) HCHO VCDs (top row), NO<sub>2</sub> VCDs (middle**  
 872 **row), and resulting VCD FNRs at  $0.1^\circ \times 0.1^\circ$  latitude  $\times$  longitude grid cells. Values of FNRs are displayed only for polluted**  
 873 **regions (NO<sub>2</sub> VCD  $> 1.2 \times 10^{15}$  molecule cm<sup>-2</sup>). The white color indicates data gaps or oceanic grid cells.**

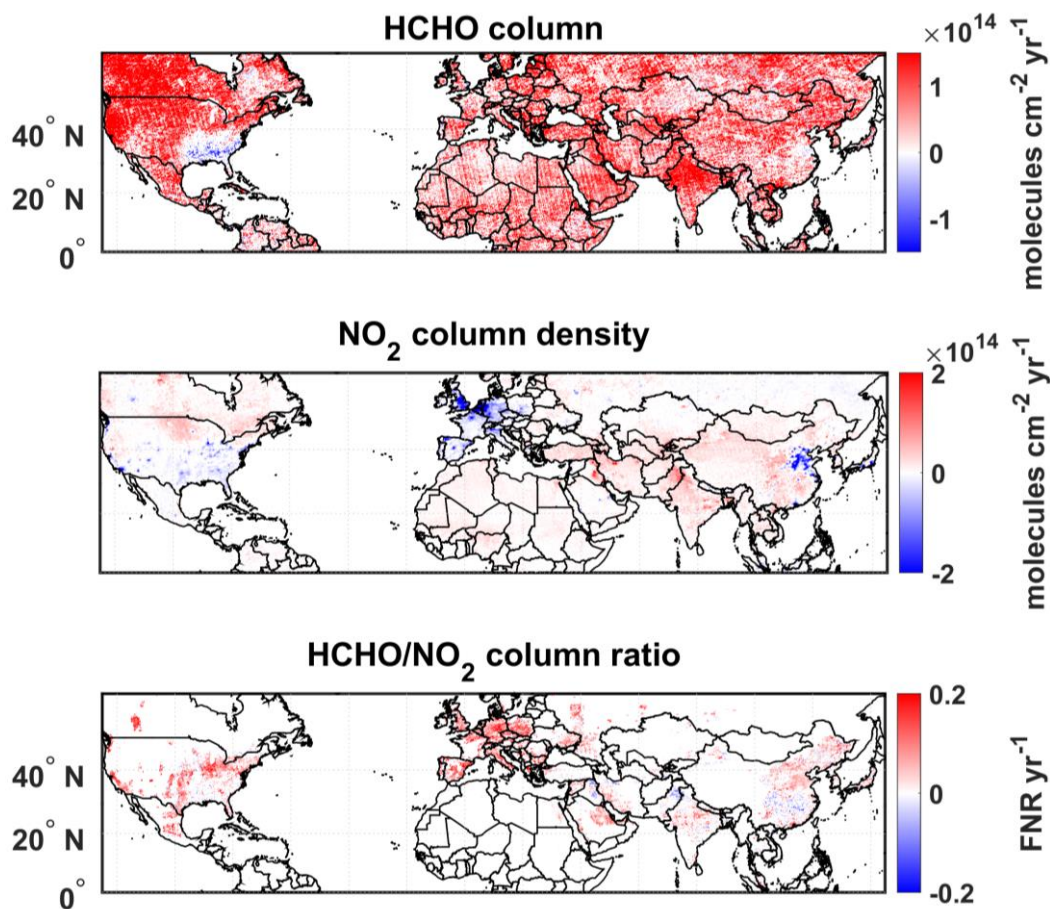
874



875

876 **Figure 2: Normalized time series (values from 2005 to 2019 normalized to 2005-2019 mean) of summer mean OMI HCHO**  
 877 **and NO<sub>2</sub> VCDs and column FNRs (solid lines). The same information is shown for surface concentrations from the EPA-**  
 878 **AQS in situ observations (dashed lines) over select cities and over all urban monitoring sites in the United States (bottom**  
 879 **right panel).**

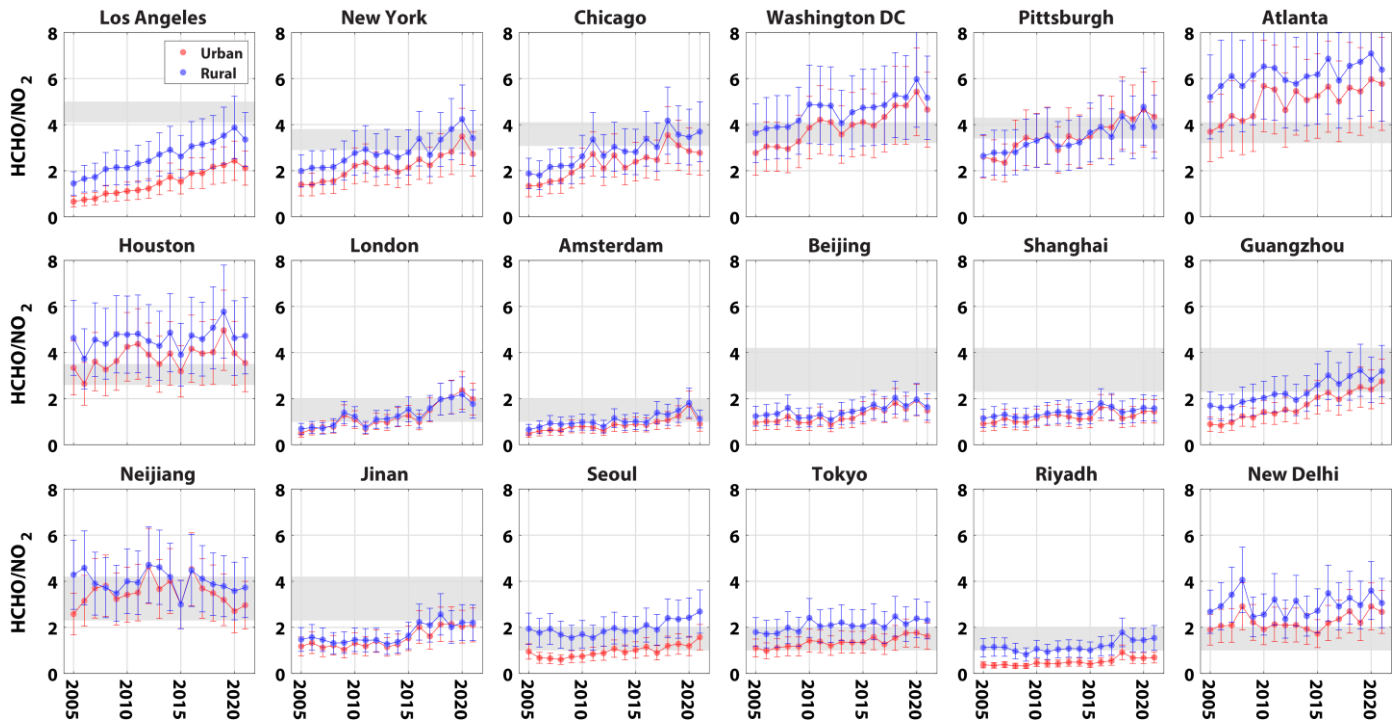
880



881

882 **Figure 3: OMI-derived trends in summer mean (June-August) time series of HCHO (top row) and NO<sub>2</sub> (middle row) VCDs**  
 883 **(units in molecule cm<sup>-2</sup> yr<sup>-1</sup>), and corresponding FNR values (bottom row; unitless yr<sup>-1</sup>) at 0.1° × 0.1° latitude × longitude**  
 884 **grid cells between 2005 and 2021. Values in the bottom row are displayed only for polluted regions (OMI NO<sub>2</sub> VCD > 1.2**  
 885 **× 10<sup>15</sup> molecule cm<sup>-2</sup>). The white color indicates data gaps or oceanic grid cells. All trend values that are displayed are at**  
 886 **an 85% confidence level ( $p \leq 0.15$ ) for better visualization of spatial trend variability. Figure S1 shows the trend values at**  
 887 **99% confidence level and for all grid cells.**

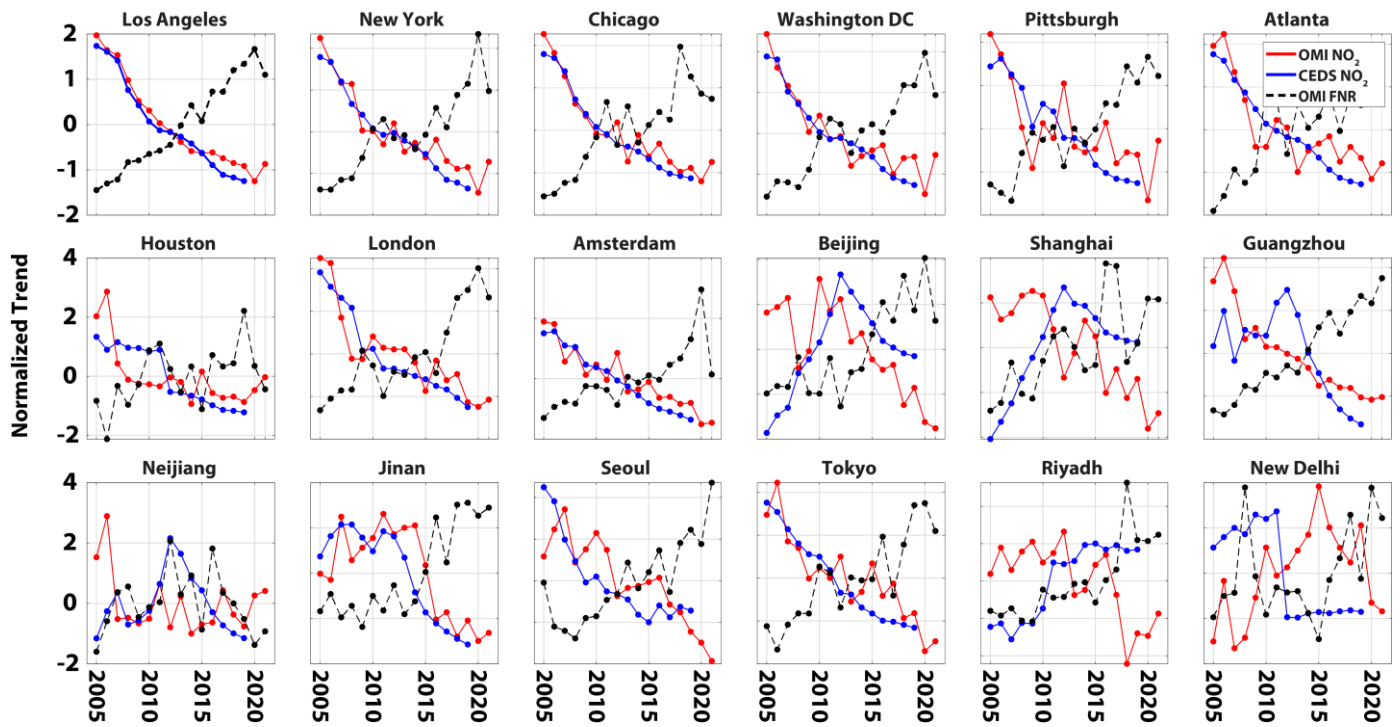
888



889

890 **Figure 4: Time series of OMI-derived summer mean (June-August) FNR VCD values for 18 selected cities across the North**  
 891 **Hemisphere from 2005 to 2021. The different colors illustrate mean FNR values for urban (red) and rural areas around**  
 892 **each city (blue). Grey shaded areas represent the transition zone of ozone production sensitivity regime threshold values**  
 893 **as suggested by Jin et al. (2020) (cities in United States: Los Angeles, New York, Chicago, Washington DC, Pittsburgh,**  
 894 **Atlanta and Houston), Wang et al. (2021) (cities in China: Beijing, Shanghai, Guangzhou, Neijiang and Jinan), and Duncan**  
 895 **et al. (2010) (other cities). For interpretation, FNR values that are less than the transition zone have O<sub>3</sub> production which**  
 896 **is VOC-limited and FNR values larger than the transition zone have O<sub>3</sub> production which is NO<sub>x</sub>-limited.**

897



898

899 **Figure 5: Time series of normalized OMI-derived summer mean (June-August) VCD NO<sub>2</sub> and FNR trend values and**  
 900 **corresponding trends in anthropogenic emission of NO<sub>x</sub> from the CEDS bottom-up inventory over the selected 18 cities**  
 901 **across the Northern Hemisphere from 2005 to 2021. CEDS emissions data is only displayed until 2019 due to this being the**  
 902 **most recent year of availability.**

903



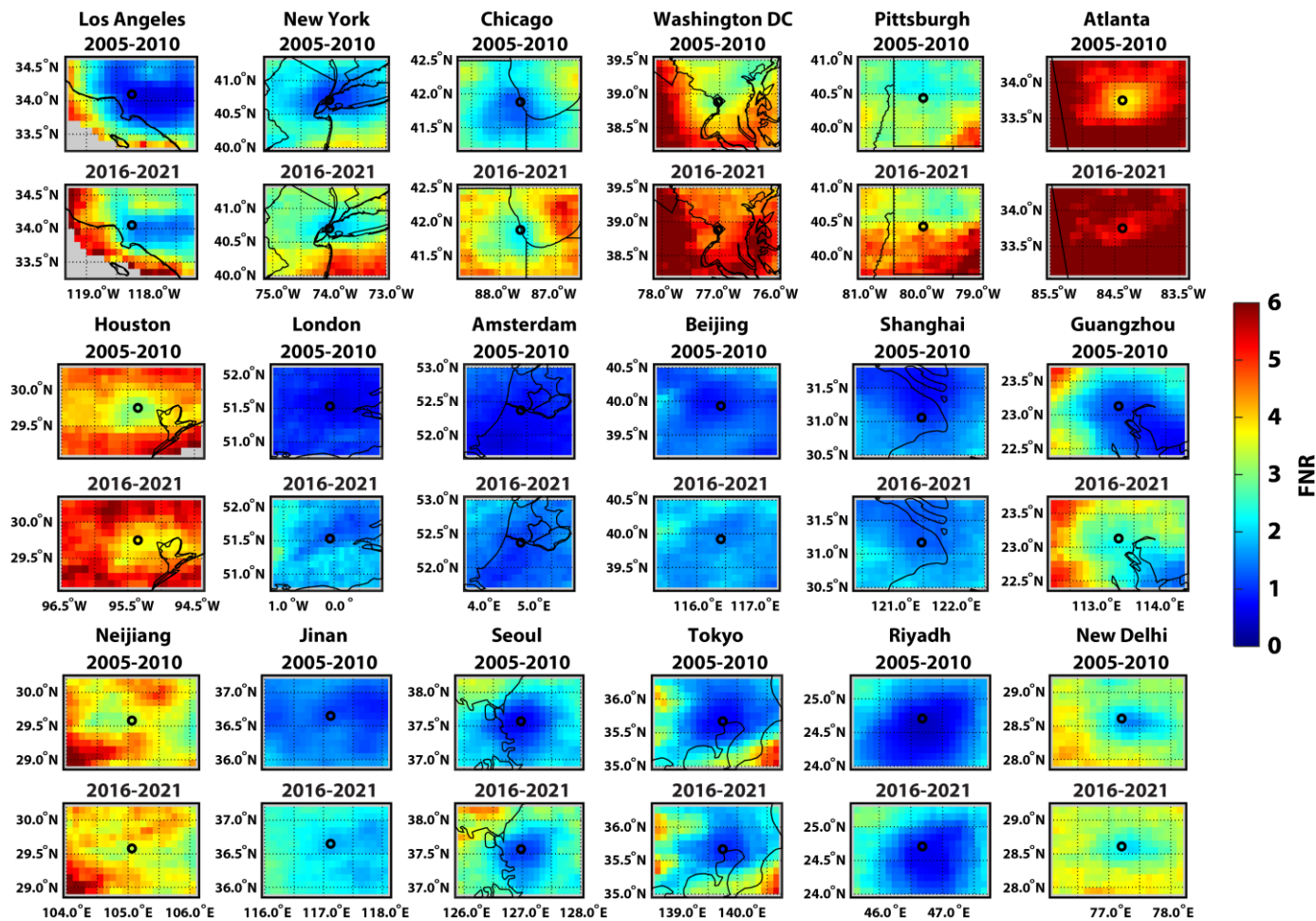
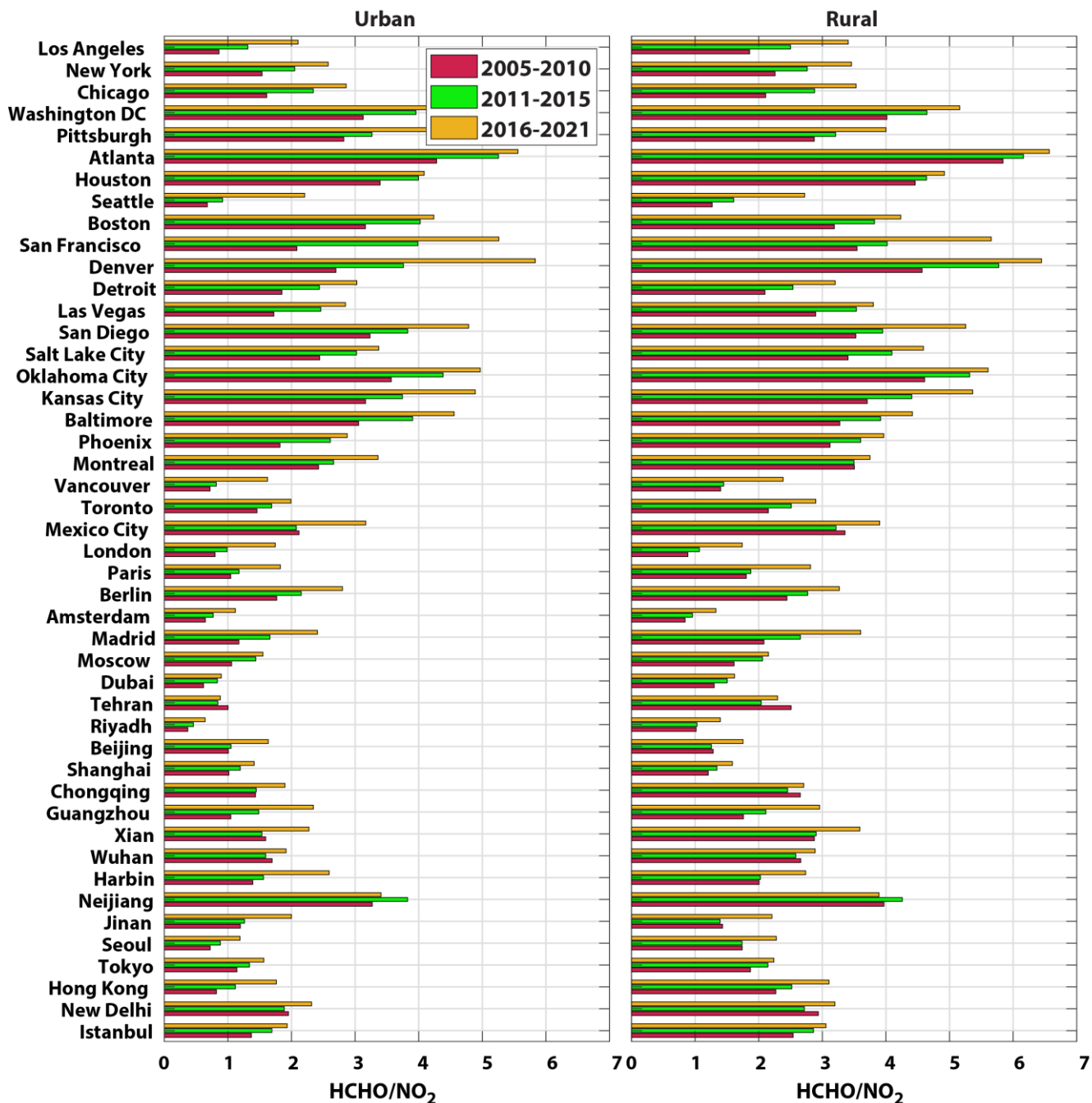


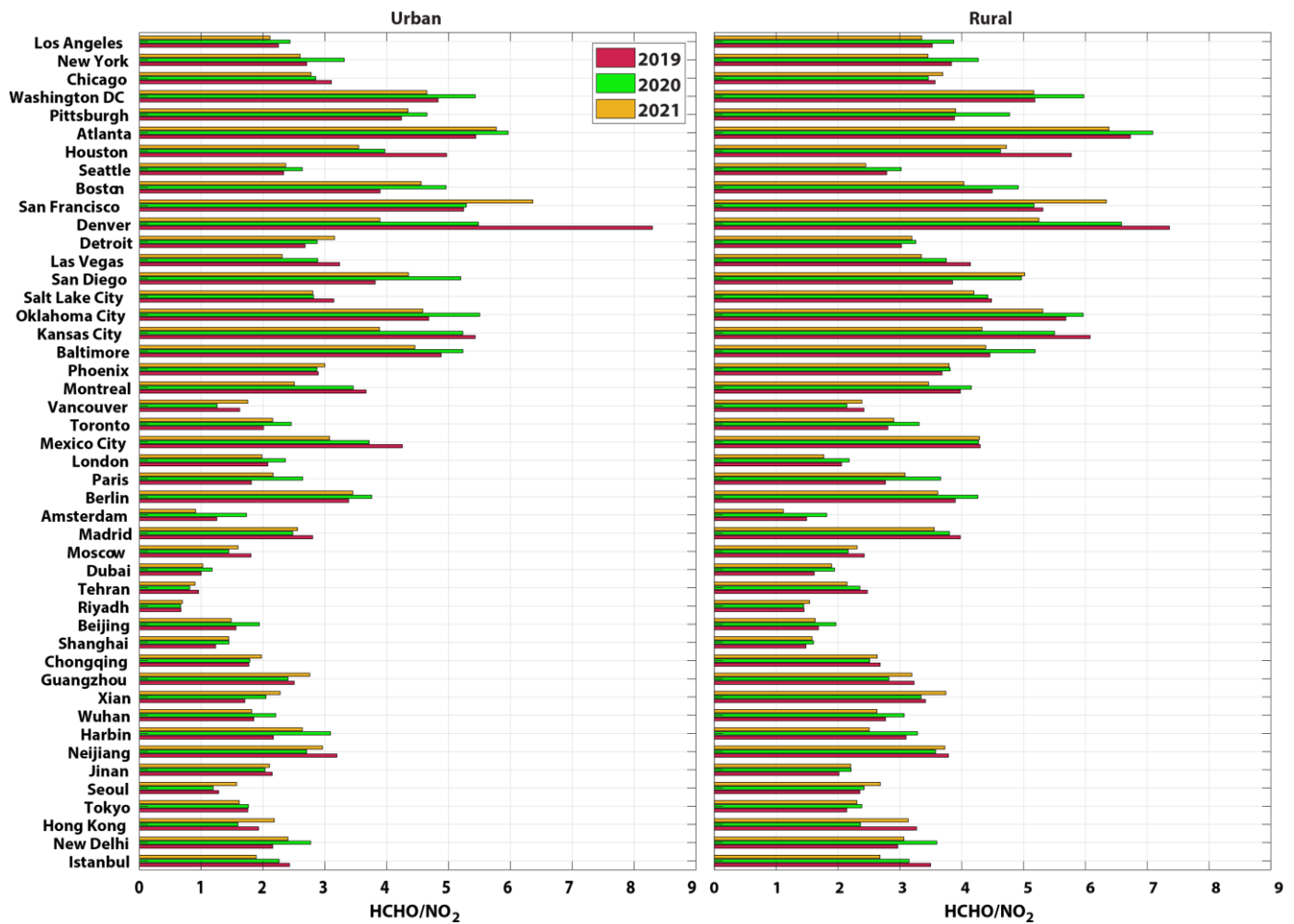
Figure 6: OMI-derived summer mean (June-August) FNR VCD values for 18 selected cities across the Northern Hemisphere during 2005-2010 and 2016-2021. The black circle represents each city center. CGLC-MODIS-LCZ urban grids for each city are displayed in Fig. S10. Grey color indicates data gaps or oceanic grid cells.



909  
 910 Figure 7: OMI-derived summer-mean (June-August) FNR VCD values for a select 46 cities across the Northern  
 911 Hemisphere during 2005-2010 (blue), 2011-2015 (red) and 2016-2021 (orange). Each column represents mean ratio values  
 912 for urban city (left column) and the surrounding rural areas (right column).

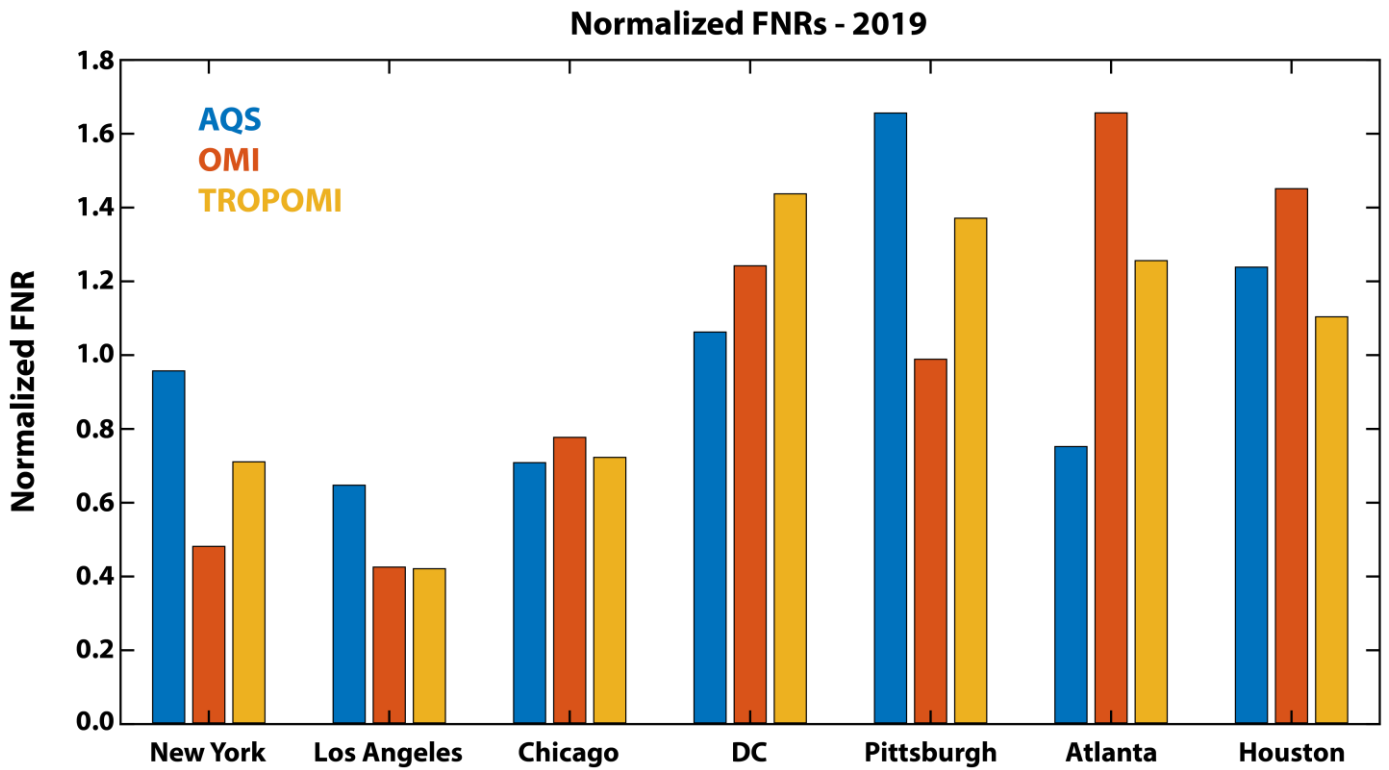
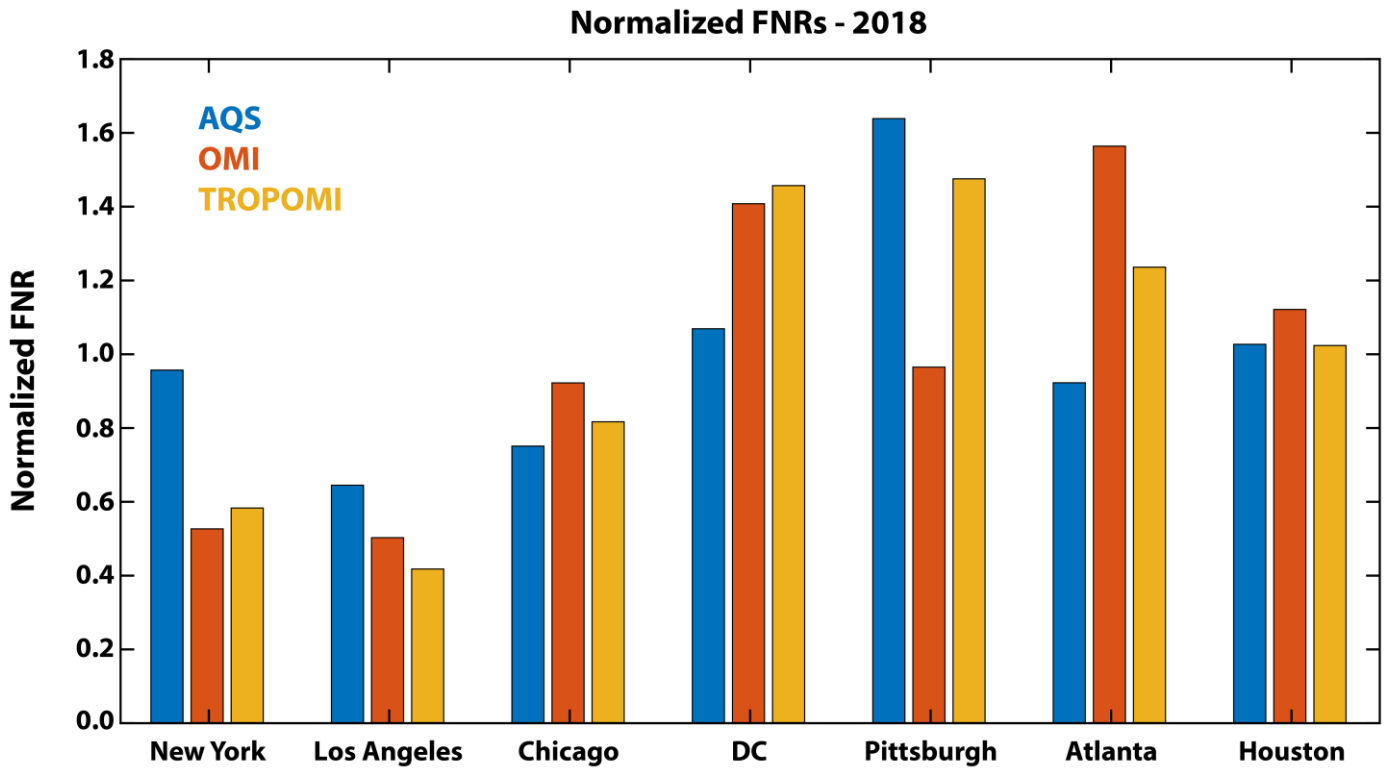
913





914  
 915 **Figure 8: OMI-derived summer-mean (June-August) FNR VCD values for a select 46 cities across the Northern**  
 916 **Hemisphere during 2019 (blue), 2020 (red) and 2021 (orange). Each column represents mean FNR values for urban city**  
 917 **areas (left column) and the surrounding rural regions (right column).**

918



919

920 Figure 9: Normalized OMI and TROPOMI summer mean FNRs (each city FNR normalized by the 7-city mean) for each of the 7  
 921 selected US cities for 2018 (top) and 2019 (bottom). The same information is shown for surface concentrations from the EPA-  
 922 AQS in situ observations over the select cities.